# Theory of Hysteresis in Halide Perovskites by Integration of the Equivalent Circuit

Juan Bisquert,* Antonio Guerrero, and Cedric Gonzales

Read Online

ACCESS | Metrics & More | Article Recommendations | SI Supporting Information

**ABSTRACT:** Perovskite solar cells show a number of internal electronic—ionic effects that produce hysteresis in the current—voltage curves and a dependence of the temporal response on the conditions of the previous stimulus applied to the sample. There are many models and explanations in the literature, but predictive methods that may lead to an assessment of the solar cell behavior based on independent measurements are needed. Here, we develop a method to predict time domain response starting from the frequency domain response measured by impedance spectroscopy over a collection of steady states. The rationale of the method is to convert the impedance response into a set of differential equations, in which the internal state variables emerge naturally and need not be predefined in terms of a physical (drift/diffusion/interfaces) model. Then, one solves (integrates) the evolution for a required external perturbation such as voltage sweep at a constant rate (cyclic voltammetry). Using this method, we solve two elementary but relevant equivalent circuit models for perovskite solar cells and memristors, and we show the emergence of hysteresis in terms of the relevant time and energy constants that can be fully obtained from impedance spectroscopy. We demonstrate quantitatively a central insight in agreement with many observations: regular hysteresis is capacitive, and inverted hysteresis is inductive. Analysis of several types of perovskite solar cells shows excellent correlation of the type of equivalent circuit and the observed hysteresis. A new phenomenon of transformation from capacitive to inductive hysteresis in the course of the current—voltage curve is reported.

**KEYWORDS:** halide perovskites, solar cells, current—voltage, impedance spectroscopy, hysteresis
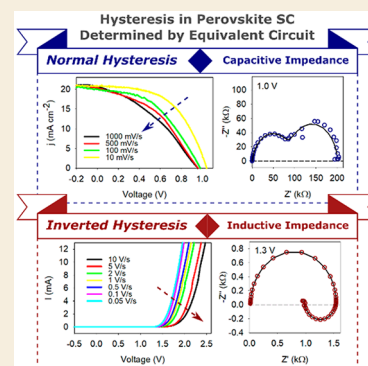
## 1. INTRODUCTION

The phenomenon of dynamic hysteresis of current—voltage curves has been present since early studies of halide perovskite solar cells (PSCs).[1−8] Hysteresis is often obtained when measuring the current of the solar cell under a voltage sweep at a constant velocity, which is a standard procedure to determine the solar cell efficiency. When the forward and reverse scans do not match, the current density—voltage curves ($J$−$V$) become separated and cast doubt on the true performance features of the devices at steady state, requiring more advanced protocols such as maximum power point tracking.[9−12] More generally, hysteresis phenomena encompass a wide variety of behaviors that depend on the applied perturbations such as scanning rate, external voltage range, and prescanning conditions. The response of PSCs is quite varied depending on the composition of the perovskite and the nature of the contacts,[13,14] and the hysteresis affects the measurement methods such as space-charge-limited currents.[15] Notably, perovskite-based devices show a significant ionic conductivity in addition to the electronic semiconductor properties.[16] The ionic influence modifies the interfaces and produces significant changes in device operation.[17] The hysteresis effect has been associated with the slow time dynamics due to ionic motion inside the perovskite layer.[16,18] There have been presented a huge number of models and explanations involving the modification of internal built-in fields, the effect of traps, and the ionic effect at the perovskite/contact interface.[18−28]

It is widely acknowledged that the hysteresis effect consists of a response of the sample that depends on the previous history and treatments. There is a strong memory effect involving one or several internal properties. It is quite difficult to make a typical mixed electronic—ionic drift—diffusion model that captures the variation of essential internal parameters under a set of experimental perturbations.[29,30] Therefore, the majority of analyses of hysteresis in PSCs are descriptions of the measurement using different types of mechanisms, often highly complex ones. These explanations typically do not have predictive power as to which circumstances, determined by independent measurements, will lead to hysteresis. It has been possible to minimize hysteresis effects in perovskite solar cells largely by empirical methods.[31−33] However, the presence of
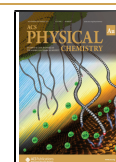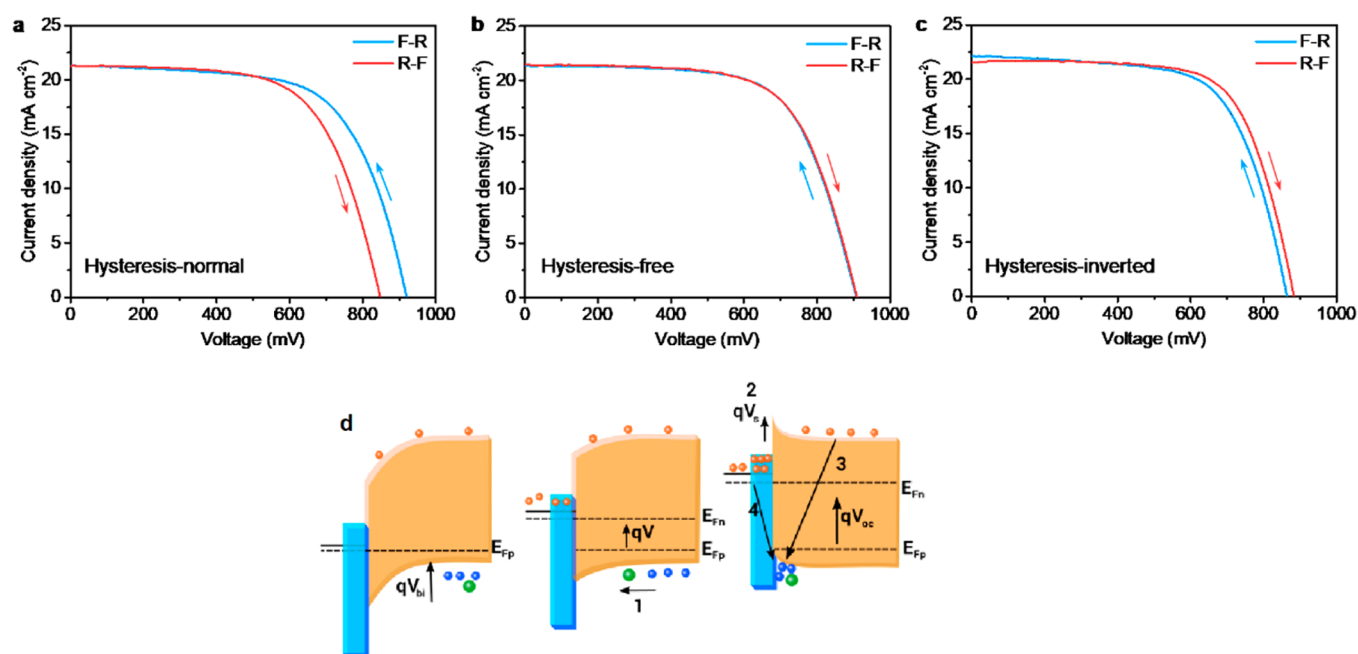
**Figure 1.** $J−V$ curves of triple-layer architecture of c-TiO$_2$/mp-TiO$_2$/ZrO$_2$/carbon hole-conductor-free printable mesoscopic PSCs with different hysteresis behaviors. (a) Hysteresis-normal device; (b) hysteresis-free device; (c) hysteresis-inverted device (F-R: from forward bias to reverse bias; R-F: from reverse bias to forward bias; scan rate 250 mV s$^{-1}$). (d) Diagram explaining the origin of hysteresis in this system: Process (1) indicates the kinetics of drift of cations and holes toward the interface. The accumulation of cations and holes at the interface creates an upward band bending which can be described by a surface voltage $V_s$ represented in (2). These accumulated charges can act as a preferential zone for both recombination with electrons in the bulk (3) and in the c-TiO$_2$/FTO region. Recombination pathway (4) is crucially dependent on the thickness of the c-TiO$_2$ layer, and is the dominant mechanism controlling recombination rates in a transient scan. Adapted with permission from ref 8. Copyright 2017 Royal Society of Chemistry.

strong hysteresis in recent high-performance configurations, such as tandem solar cells, still persists.[34−36] Therefore, new methods that provide insight into hysteresis in PSCs via alternative measurement may have significant practical value.

Here, we aim to develop a method for the analysis of hysteresis that does not need to establish a specific physical model of the solar cell. Following the techniques of electrical engineering,[37] we can predict the time evolution of the system by having information on the small perturbation response in the frequency domain, even in the case in which internal state variables present their own relaxation effects that result in memory properties.

In order to find the frequency domain response, we use the equivalent circuit (EC) model that results from the measurement of impedance spectroscopy (IS). Thereafter, we transform the EC into a set of dynamical equations in the time domain. Finally, the system of differential equations is solved as a function of time (or voltage) by integration for the required conditions and perturbations and is compared to the experimental curves. In this way, we obtain definite information on the causes of the hysteresis in the device, and we can then modify material components and measure them separately by IS.

A memristive device is a two-terminal structure that undergoes a voltage-controlled conductance change.[38] The hysteresis effects in halide perovskites facilitate the construction of effective memristors involving different mechanisms. These have been applied to resistive random access memories,[39] artificial neural networks (ANN),[40,41] and photonic memories and synapses.[42,43] The method developed in this paper will provide insight into the essential memory effects of perovskite memristor devices.

In the early years of PSC research, reproducibility was a very serious issue. In the measurement of $J−V$ curves, voltage or light pretreatments would modify the outcome significantly. Even a single measurement would change the subsequent response,[44] and it was difficult to distinguish between the varied sample-drift effects associated with the uncontrolled casuistic hysteresis-type effects or the slow degradation modifying the cell irreversibly. In particular, the measurement of impedance spectroscopy could affect the state of the sample afterward. In such conditions, it would be rather difficult to attempt to effectively relate IS results and time domain response. At the present time, we are confident that robust PSCs can be prepared in which the response of the cell is the same after measurements, such as IS and cyclic voltammetry (CV), are performed. It has become possible to test complex temporal responses connected to frequency domain measurements. It is time to develop a robust theory that captures the essential physical elements of hysteresis.

Let us define the phenomenon that we want to study. Figure 1 shows the $J−V$ curves of three perovskite solar cells that differ only slightly by the thickness of the compact TiO$_2$ layer at the contact in highly stable triple layer carbon PSC.[8] The $J−V$ curve is the essential characteristic to evaluate the performance of the solar cell. It requires a sweep of voltage from reverse to forward voltage (forward scan) or from forward to reverse voltage (reverse scan direction). Figure 1a shows that the forward scan exhibits a lower current and voltage than the reverse scan. This is a normal hysteresis. In Figure 1c, the opposite situation occurs, and it is called inverted hysteresis. In Figure 1b, the forward and reverse scans give the same result. In this case, it is said that hysteresis has been suppressed. In Figure 1d, an energy diagram explains the

observed hysteresis effects in terms of physical mechanisms such as migration of ions to the surface, modification of band bending, and influence on recombination. In the present paper, we will propose a different type of understanding of hysteresis based on the interpretation of the impedance spectroscopy spectra and the associated EC.

In the next section, still introductory, we describe major trends of the hysteresis in PSCs, as well as the general properties of the observed response in the frequency domain. Two basic but important EC models are introduced that will serve us, thereafter, to establish the correspondent behavior under cyclic voltammetry, revealing the connection between hysteresis and the EC. In the final section, we revise a set of experimental results on impedance spectroscopy and hysteresis in different PSCs that show a sound correlation, as predicted by the theory, and reveal new properties of time constants and ECs providing deep insight into the time domain behavior of perovskite solar cells.

## 2. BACKGROUND OF IMPEDANCE SPECTROSCOPY AND HYSTERESIS

### 2.1. Impedance Spectroscopy

The technique of impedance spectroscopy is amply used for the characterization of emergent solar cells[45,46] and PSCs.[17,47,48] The electrical variables are the current $I$ and voltage $V$ measured at the contacts. The linear small perturbation variables associated with ac modulation amplitude bear a tilde, $\tilde{I}(\omega)$ and $\tilde{V}(\omega)$, whereas those associated with a steady state where the measurement was made bear an overbar, $\bar{V}$. The impedance is defined with respect to measurement of small perturbation signals at angular frequency $\omega$, over a steady state at the operational point $\bar{I}(\bar{V})$:

$$Z(\omega) = \frac{\tilde{V}(\omega)}{\tilde{I}(\omega)} \tag{1}$$

Figure 2a shows the process of measurement of the impedance in terms of the small perturbations, and Figure 2b incorporates an internal variable $w$ that will be discussed in the later sections.

The impedance can be presented in terms of the real and imaginary parts:

$$Z(\omega) = Z'(\omega) + iZ''(\omega) \tag{2}$$

The complex capacitance $C(\omega)$ is defined from the impedance as

$$C(\omega) = \frac{1}{i\omega Z(\omega)} \tag{3}$$

It can be separated into real and imaginary parts as

$$C(\omega) = C'(\omega) - iC''(\omega) \tag{4}$$

In Figure 3, we show characteristic measurements of the IS response of PSCs when the conditions of illumination or photovoltage are modified, producing large changes in the parameters. In Figure 4, we show the EC model that has been amply used to fit the optimized PSC devices.[49,50] The circuit element $C_g$ is the geometrical capacitance corresponding to dielectric polarization in the bulk, and $C_1$ is the large low-frequency (LF) capacitance associated with the generation of the ionic double layer in the vicinity of the contacts.[47,51] The capacitance–frequency plot (Figure 4b) shows a plateau at high frequencies (HF) corresponding to $C_g$ and increase
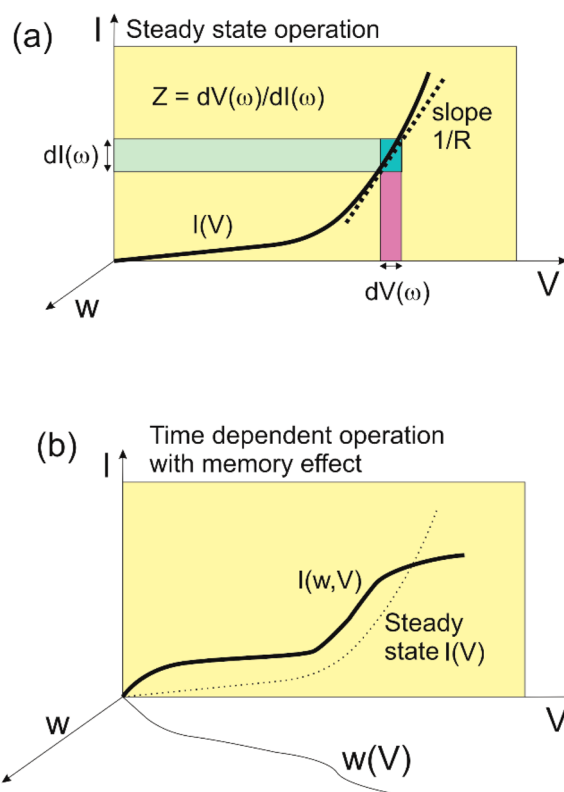


**Figure 2.** (a) Scheme of a current–voltage ($I$–$V$) curve indicating the measurement of small perturbation voltage and current that provide the impedance $Z$. At low frequency, the slope of the $I$–$V$ curve is the reciprocal resistance. (b) In the presence of the memory internal variable $w$, the actual $I$–$V$ curve depends on the evolution of $w$. The curve departs from the steady-state curve and shows hysteresis.

toward the LF value, where the slow kinetics of $C_1$ becomes activated. The real part of the capacitance calculated from eq 3 at LF is

$$C'(\omega = 0) = C_g + \left(\frac{R_1}{R_1 + R_3}\right)^2 C_1 \tag{5}$$

The two arcs in Figure 3a and 4a are associated with two resistances. We denote the LF arc resistance as $R_1$ (the parallel connection of $R_1$ to $C_1$ generates the LF arc) and the HF resistance as $R_3$. The meaning of the resistances depends on the illumination conditions, but the LF arc usually relates to the perovskite/contact interface (ion migration, accumulation, and recombination).[52]

We note that from the fitted parameters under open-circuit conditions in Figure 3b,c, the geometric capacitance is basically constant, but the other three parameters in the EC show an exponential dependence with the voltage (Figure 3d);[53] therefore, they may be expressed as

$$R_1(V) = R_{10}e^{-qV/m_1 k_B T} \tag{6}$$

$$C_1(V) = C_{10}e^{qV/m_C k_B T} \tag{7}$$

$$R_3(V) = R_{30}e^{-qV/m_3 k_B T} \tag{8}$$

where $V$ is the solar cell voltage, $q$ is the elementary charge, $k_B T$ is the thermal energy, and $m_i$ is an ideality factor for each parameter. In the case of band-to-band recombination, it is $m = 1$.[54] The values indicated in Figure 3c,d are $m \approx 2$ in all cases.
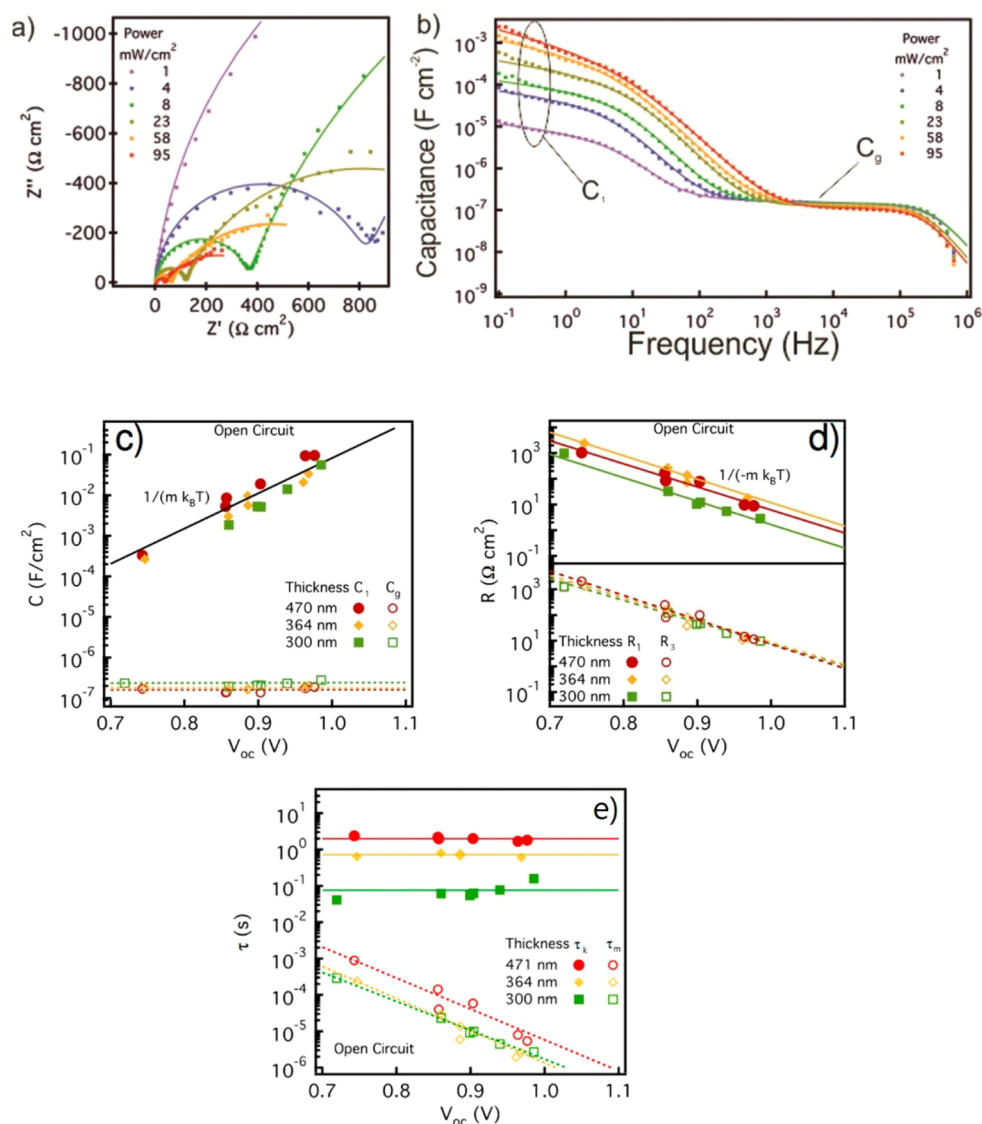
**Figure 3.** Impedance spectroscopy results of a planar structure FTO/TiO$_2$/MAPbI$_3$/spiro-OMeTAD/Au solar cell. (a) Example of complex plane impedance plot measured under short-circuit conditions at different irradiation intensities. (b) Example of capacitance spectra corresponding to the conditions in panel (a). Solid lines correspond to fits using the EC. (c) Capacitances and (d) resistances under open-circuit conditions. Solid lines (low-frequency arc) and dashed lines (high-frequency arc) correspond to linear fits with $m$ approaching 2. In panel (c), $m = 1.90 \pm 0.17$, and in panel (d), $m = 1.94 \pm 0.08$. (e) Response time calculated from the RC product for the low-frequency arc (solid line) and high-frequency arc (dashed line). Reproduced from 49. Copyright 2016 American Chemical Society.

It is remarkable that the two elements of the low-frequency arc are strongly correlated, $m_C \approx m_1$, so that the response time for the slow relaxation phenomenon is a constant independent of the voltage:[47,49,55]

$$\tau_1 = R_1 C_1 \tag{9}$$

This is observed in Figure 3e. It should be mentioned that these good correlations are obtained measuring each voltage point at open circuit, in the absence of background current.

In contrast to this, the high-frequency relaxation time

$$\tau_m = R_3 C_g \tag{10}$$

is not constant and follows the trend of $R_3(V)$.

By definition, memristor devices undergo strong memory effects and become interesting platforms for the analysis of hysteresis. Perovskite interfacial conductivity can be controlled by the ionic displacement and reaction, giving rise to

memristive devices.[56,57] A similar two-arc response as in PSCs has been observed in perovskite-based memristor devices at low applied voltages.[57] Figure 5 shows the current−voltage loops in the dark of a memristor based on 2D halide perovskite with a Ag contact layer. The device shows a strong memory effect that causes the forward and reverse scan to be well-separated, even at slow scan rates. This is associated with the construction of a conductive ionic layer at the Ag contact.[56,57] Note that Figure 5 can be viewed as a huge inverted hysteresis of the type of Figure 1c, with the corresponding semilog I−V curve shown in Figure 6a. In the impedance spectroscopy response at low voltages in Figure 6b, the same types of two-arc spectra are observed as in Figure 3.[57] However, when the memristor approaches the voltage of the transition to a low resistance state (LRS), that is, at about 0.5 V, a new feature appears in which the LF arc reduces size and enters the fourth quadrant of the complex plane, as shown in the enlarged view
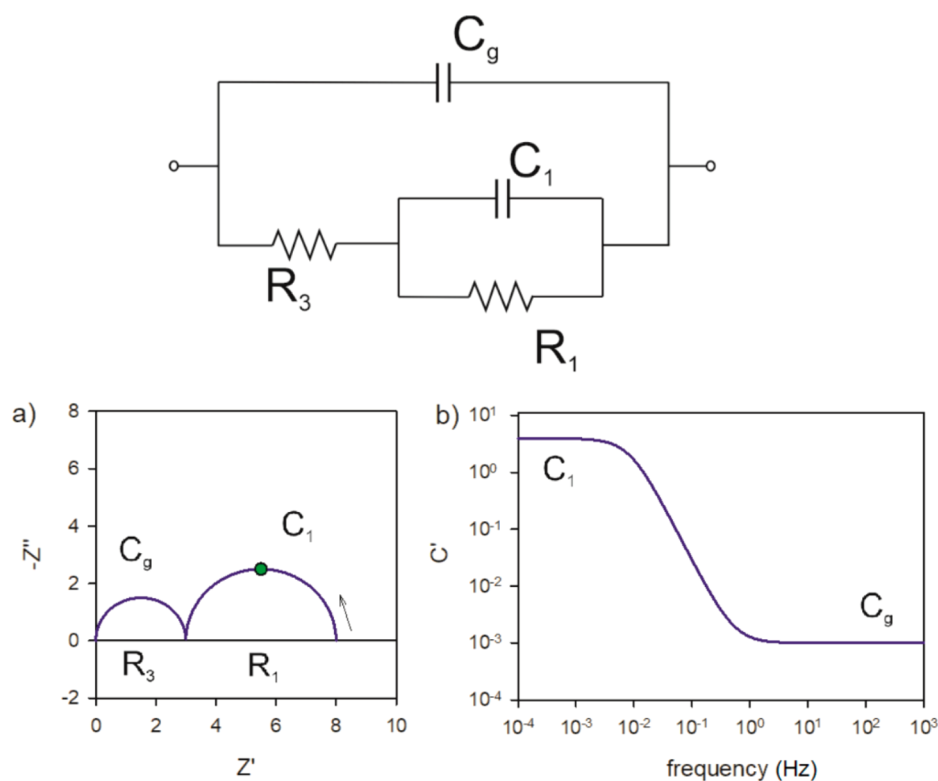
**Figure 4.** Equivalent circuit and (a) complex plane impedance spectrum (impedances in $\Omega$). The arrow indicates the direction of increasing frequency. The point indicates the angular frequency $1/\tau_1 = 1/R_1 C_1$. (b) Real part of the capacitance versus frequency. Parameters $R_1 = 5\ \Omega$, $R_3 = 3\ \Omega$, $C_1 = 10$ F, $C_g = 10^{-3}$ F.
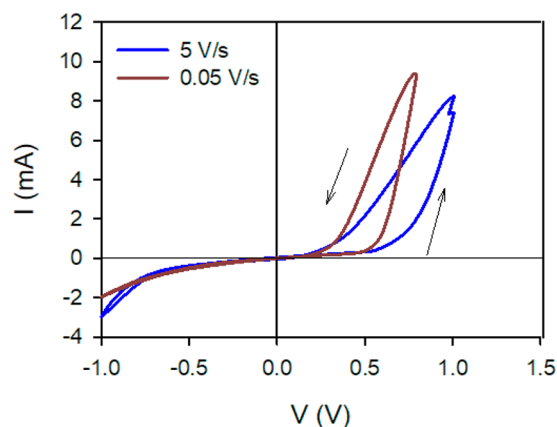


**Figure 5.** Current−voltage scans of a FTO/PEDOT:PSS/2D Ruddlesden−Popper perovskite/Ag (15 nm)/Au (85 nm) memristor device in the dark at different scan rates.

in the inset of Figure 6b. This behavior consisting of a "hook" at low frequency has been observed in many of the halide perovskite solar cells.[58−61] The EC model shown in Figure 7 contains a single RC process coupled to an RL line that describes the hook shape. In terms of the Laplace variable $s = i\omega$, the impedance of Figure 7 takes the form

$$Z(\omega) = [R_b^{-1} + C_m s + (R_a + L_a s)^{-1}]^{-1} \qquad (11)$$

Depending on the values of the circuit parameters, the impedance can show an inductive loop or not, as noted in the different types of spectra in Figure 7a,c,d. The parallel RL line has been proposed in the literature in relation to the negative capacitance observed in solar cells (Figure 7b).[62,63] The

inductive loop describes a general memory effect, and it has been observed in metal oxides,[64] in LiNbO$_2$ memristors,[65] and in proton exchange membrane (PEM) fuel cells.[66] In PSC, it can be justified from a recent kinetic model,[67,68] in which an internal surface voltage that is slowed down by ionic motion relaxes to the quasi-equilibrium state imposed by the external voltage $V$ applied to the solar cell.

In terms of the EC, the operation of the memory mechanism consists of modifying the overall resistance of the system as a function of the frequency. At high frequency, the impedance of the inductor is very large and $R_a$ does not contribute to the response. When the frequency is reduced, the impedance of the inductor vanishes progressively, and the loop in the fourth quadrant reduces the overall resistance of the system.

A related issue that has been intensely discussed in the area of PSC is the meaning of the often observed negative capacitance[59,60,62,63,69−72] that causes great uncertainty of interpretation. We remark that the EC of Figure 7 consists of a positive inductor not a negative capacitor. However, as shown in Figures 3 and 4, it is useful to plot the capacitance versus the frequency. In the calculation of the real part of the capacitance by eq 3, the positive inductor RL line produces a negative capacitance effect (Figure 7b). This is a customary denomination, but there are no negative elements in this model.

An EC such as those in Figures 4 and 7 is not unique. It allows a number of possibilities of alternative expressions.[73] The adoption of a particular EC model is based on the physical interpretation of the elements based on experiments in different configurations of the solar cell.
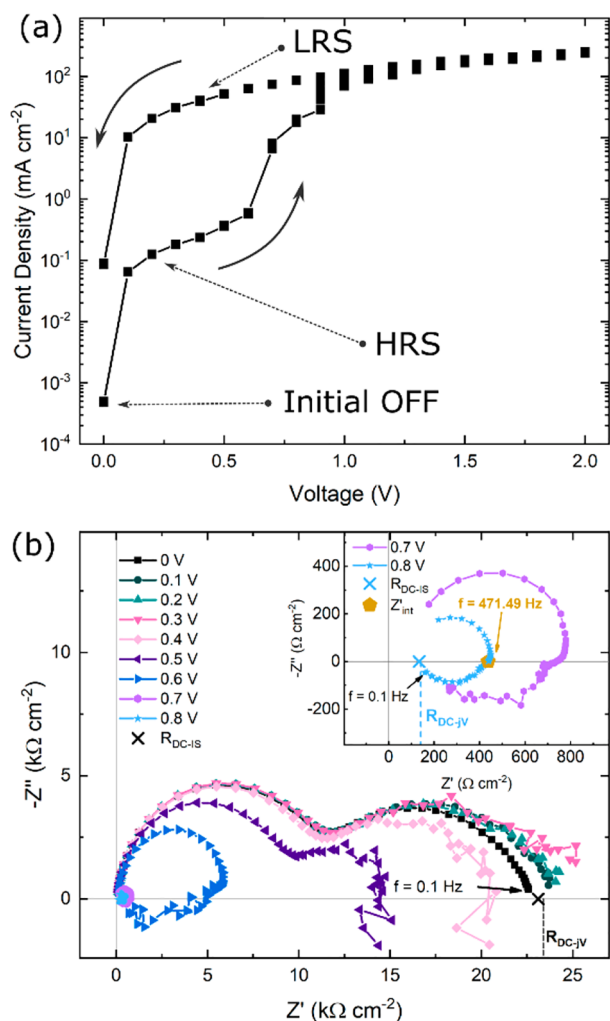
**Figure 6.** (a) Semilog current−voltage curve of a FTO/PEDOT:PSS/ 2D Ruddlesden−Popper perovskite/Ag (15 nm)/Au (85 nm) memristor device showing the transition from high resistance state to low resistance state. (b) Impedance spectroscopy spectra evolution of the memristor at representative voltages. Reprinted with permission from ref 57. Copyright 2021 American Institute of Physics.

### 2.2. Relation between IS Values and *J*−*V* Curve

We show the connection of the *J*−*V* curve to the impedance *Z* with a simple example. Figure 2a shows the small amplitude perturbation quantities in a point of the steady-state curve. Here, we restrict the analysis to the stationary condition, $\omega = 0$, and the impedance reduces to the dc resistance:
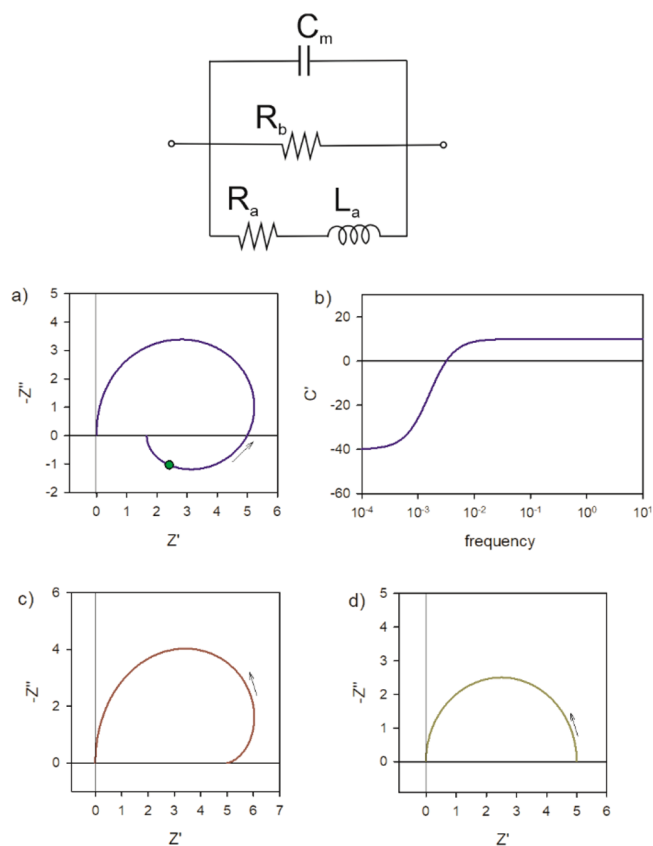
$$Z = R_{dc}(V) \tag{12}$$

These small amplitudes of the electrical perturbations can be treated as differentials, $\tilde{I}(\omega) \rightarrow dI$, $\tilde{V}(\omega) \rightarrow dV$. Hence eq 1 becomes

$$dI = \frac{1}{R_{dc}(V)}dV \tag{13}$$

As shown in Figure 2a, $R_{dc}(V)$ is the reciprocal slope at each point of the curve. Let us suppose we measure the impedance at different voltages, and we arrive at the form

$$R_{dc}(V) = R_{dc0}e^{-qV/mk_BT} \tag{14}$$



**Figure 7.** Equivalent circuit including an inductive branch and the associated complex plane impedance spectra. (a) $R_a = 2$, $R_b = 10$, $C_m = 10$, $L_a = 200$, (c) $R_a = 10$, $R_b = 10$, $C_m = 10$, $L_a = 1000$, (d) $R_a = 2$, $R_b = 10$, $C_m = 100$, $L_a = 100$. The arrow indicates the direction of increasing frequency. (b) Real part of the capacitance of the system parameters in (a). The highlighted point in (a) is at the angular frequency $1/\tau_k = R_a/L_a$.

Inserting eq 14 into 13 and performing the integration, we obtain the diode equation of the solar cell:

$$I(V) = \frac{mk_BT}{qR_{dc0}}(e^{qV/mk_BT} - 1) \tag{15}$$

This trivial example shows that current voltage curve is linked to impedance spectroscopy by an integration. Our objective is to develop a general integration method valid for any EC and for all the frequencies related to a certain stimulus in the time domain represented by a specific applied voltage schedule $V(t)$.

### 2.3. Properties of Hysteresis in Halide Perovskite Devices

Figure 8 shows the measurements of the *J*−*V* curve at a constant voltage sweep rate by following a ramp of voltage at successive voltage steps. When the steps take a long duration of 1 s, the forward and backward results are the same (Figure 8a). However, for faster steps of duration 0.1 s, the relaxation to an equilibrium value has not been yet completed when the new step comes in. Hence, the scan in the forward direction shows currents lower than those of the stationary curve, and the scan in the reverse direction shows larger currents (Figure 8b). Figure 8c shows that the amount of hysteresis increases with the scan rate. The opening of the curve can be quantified by a hysteresis index defined by the change of a given property of the *J*−*V* curve with respect to the velocity parameter.[74] This is useful to track the evolution of the hysteresis with some
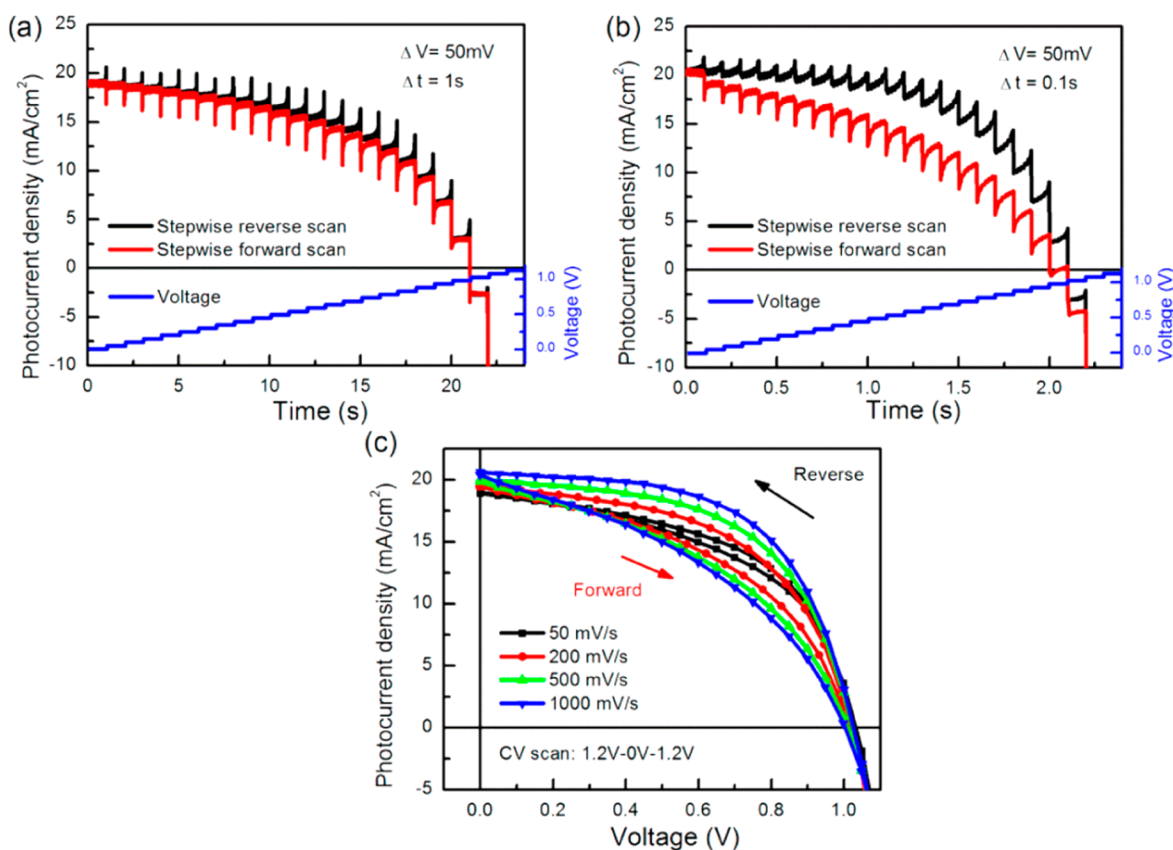
**Figure 8.** Time-dependent photocurrent response of planar perovskite solar cell on compact $TiO_2$ (cp-$TiO_2$) with 500 nm $CH_3NH_3PbI_3$ film as the light-absorber layer and 150 nm spiro-OMeTAD as the HTM layer under reverse and forward stepwise scans with (a) 1 s step time and (b) 0.1 s step time. (c) $J-V$ response for PSCs with different CV scan rates. Reproduced from ref 7. Copyright 2015 American Chemical Society.

internal or external parameter, as the thickness of a layer in the solar cell (Figure 1) or the humidity (Figure 11).

In Figure 8b, we can see that the overall hysteresis response can be obtained as a sum of the results of small perturbation steps. This is the essence of the integration method in a kinetic situation that will be developed below: we will establish the same procedure mathematically.

It has been widely recognized that there is a strong connection between IS properties and the hysteresis features of PSCs. More concretely, the capacitive effect is well-recognized to be associated with hysteresis.[7,75−77] The capacitive current increases with scan rate in forward direction[78] and changes sign when the direction of the scan is inverted, as shown in Figure 9a. Since Figure 9a shows the change of the dark current, it is related to a decrease of photocurrent in forward scan, as shown in Figure 1a. This is termed *capacitive current* in a general sense. In contrast, no capacitive current is observed for an inverted contact structure device in Figure 9b.

As an example of the correlation of capacitance and hysteresis, Figure 10 shows[5] the effect of capacitive hysteresis in two PSCs: one cell with $TiO_2$ contact (Figure 10a) and a low-capacitance PSC with organic electron selective contact.[13,14] The cell with $TiO_2$ contact displays a large capacitance at low frequency in both dark and illuminated conditions (Figure 10d,e). Hysteresis in this cell is much larger than that in the cell with the organic contact (Figure 10b). In addition, the time-dependent short-circuit current, $J_{sc}$, of the normal structure exhibiting the severe normal hysteresis shows

an exponential decay attributed to the accumulated capacitive current (Figure 10c).[5]

We have commented that in Figure 1c a different behavior is observed. The forward scan increases the photovoltage, and this is called inverted hysteresis.[8,23,79] Note in Figure 9b that, in a voltage sweep, the current changes in the opposite way to the capacitive variation. By the relation of noncapacitive currents (Figure 5 and Figure 9b) and the inductor element, we may speak of *inductive hysteresis* (inverted) versus *capacitive hysteresis* (regular). Indeed, the connection between the inductive branch of the impedance results and the inverted type of hysteresis in PSCs has been exposed by Fabregat-Santiago and co-workers, as shown in Figure 11.[80] They have associated the presence of the inductive loop (Figure 11c,d) to a negative hysteresis index (Figure 11b) that indicates an inverted hysteresis (Figure 11a). However, a physical explanation for this connection between time and frequency domain results has not been elaborated. In the context of our methods developed below, we will show a clear scheme for this correlation.

## 3. METHOD TO DESCRIBE HYSTERESIS FROM THE EQUIVALENT CIRCUIT

We start the description of the methodology to describe hysteresis features based on information in the frequency domain.

The general operation to switch between time and frequency domain is the Laplace transformation and its inverse, according to the desired direction. However, in the case of the
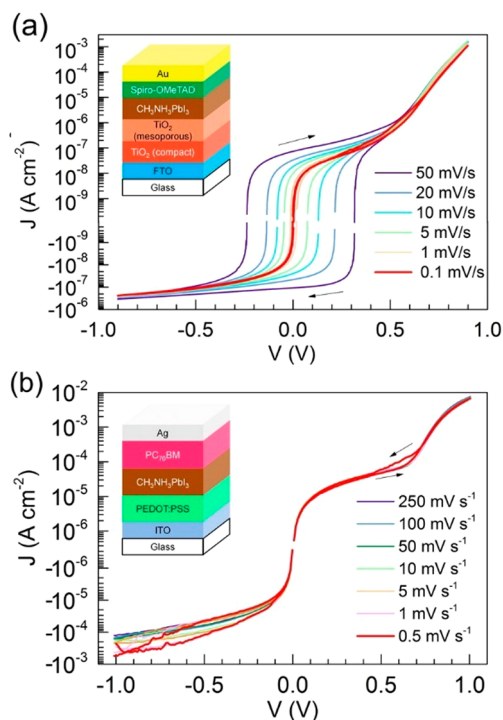
**Figure 9.** Dark $J{-}V$ curves at room temperature in logarithm scaled current representation: (a) Regular mesoporous PSC and (b) inverted PSCs at different scan rates with corresponding structures illustrated in the insets. Reproduced from 6. Copyright 2016 American Chemical Society.

experimental methods used to measure solar cells and related devices, the connection between time and frequency domain is not obvious.

In the measurement of the impedance spectra of Figure 3a, the system has been stabilized at a steady state, and the linear response $Z(\omega)$ is obtained by very small voltage amplitudes d$V$ (Figure 2a). In contrast, for the measurement of CV, the voltage makes a large excursion of about 1 V, as shown in Figure 8, at a scan rate $v_0$ according to the expression

$$V(t) = V_0 + v_0 t \tag{16}$$

Typical sweep voltage rates start at 10 mV/s up to 100 V/s or more. In the fast voltage sweep, the physical processes in the sample are not sitting close to a quasi-equilibrium state, and the full nonlinearity and memory effects come into play, determining the response to the perturbation. We can invent a model based on detailed internal mechanisms that produces the required observed responses: electrical fields, ions situated in the wrong side of the polarization that screen the field, interfacial traps, surface barriers that change by photogenerated charges that pile up at the barrier, enhanced recombination in the absorber, and so on. However, each model can be arbitrary to a large extent requiring plenty of explanations. Our goal is to provide a methodology to pass directly from the impedance response obtained at the different voltages of the range of measurement to the large perturbation response like that in eq 16.

It seems hopeless at first sight since the information that we have is represented by an impedance function like eq 11 and the voltage dependence of the circuit elements obtained from fitting the spectra at different steady states. However, very often, the linearized response contains significant information
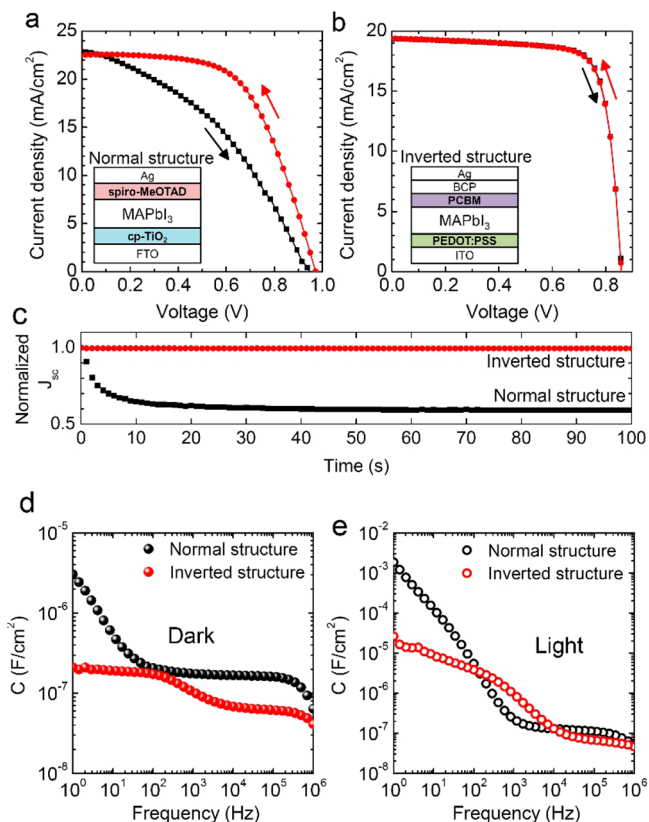


**Figure 10.** (a) $J{-}V$ hysteresis of the cp-TiO$_2$/MAPbI$_3$/spiro-MeOTAD (normal) structure and (b) PEDOT:PSS/MAPbI$_3$/PCBM (inverted) structure. During the $J{-}V$ scan, the current was acquired for 100 ms after applying a given voltage. (c) Normalized time-dependent short-circuit current density ($J_{sc}$) of the normal and the inverted structures. Open-circuit condition under one sun illumination was maintained before measuring $J_{sc}$. Capacitance–frequency ($C{-}f$) curves (d) under dark and (e) one sun illumination at short-circuit condition (bias voltage = 0 V). Reproduced from ref 5. Copyright 2015 American Chemical Society.
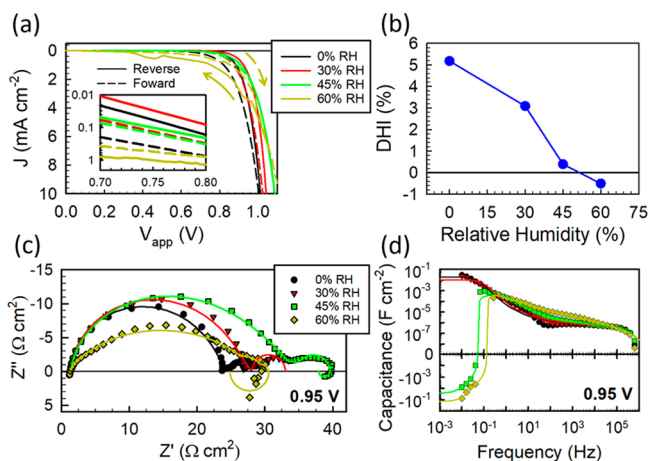


**Figure 11.** Measurements of regular MAPbI$_3$ solar cells (FTO/TiO$_2$/mp-TiO$_2$/MAPbI$_3$/spiro-OMeTAD/Au) at different relative humidity values (0, 30, 45, and 60%) under dark conditions. (a) CV curves and (b) their respective hysteresis index. (c) Impedance plots with (d) corresponding capacitance spectra at 0.95 applied voltage. Solid lines correspond to fits using the EC including a RL branch. Reproduced from ref 80. Copyright 2020 American Chemical Society.
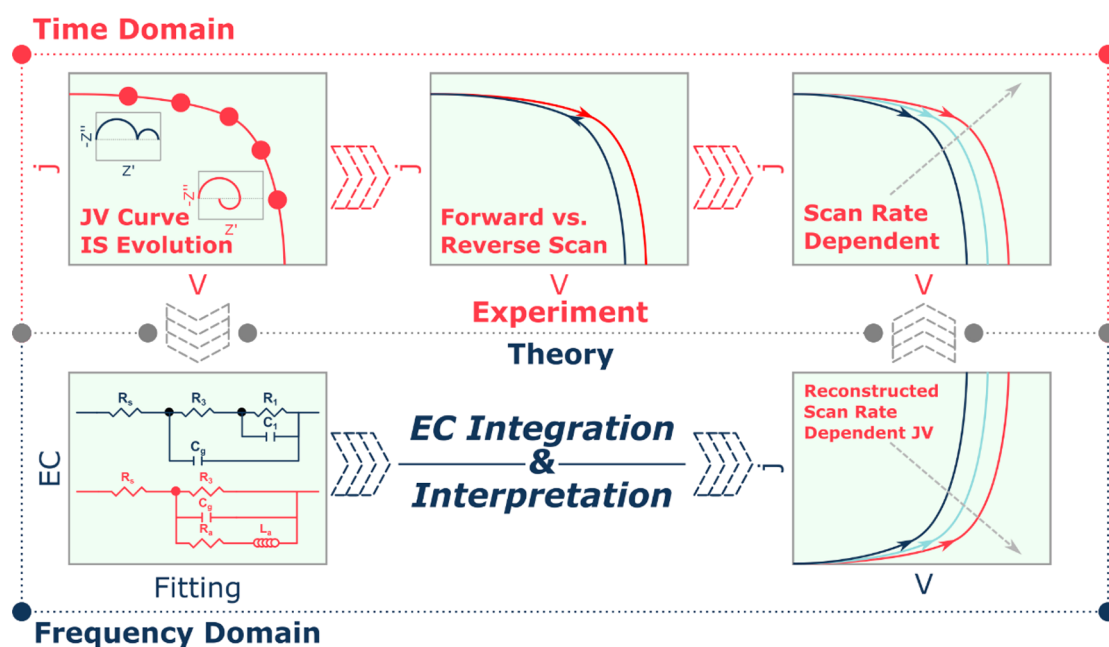
**Figure 12.** Integration scheme of the EC from frequency domain to time domain.

about the response to a large-scale perturbation. These methodologies are widely used in electrical engineering,[37] in stability and bifurcation,[81,82] and for the analysis of oscillating systems based on impedance spectroscopy.[83,84] These methods define a dynamical system by a set of differential equations that refer to external variables applied to the system, that is, current $I$, voltage $V$, illumination, and a set of internal state variables $w_i$ that correspond to the relevant evolving quantities that determine the internal evolution with time. By stating an initial condition to all the variables, the differential equations allow one to predict the evolution of the system.

It is well-recognized that impedance spectroscopy has a great advantage in allowing separation of internal processes that determine the overall spectral response, for example, manifested as two neatly distinguished arcs in Figure 3a. The central tool to obtain an interpretation of the impedance response is to establish an EC model. Then we can represent the system's response by the voltage dependence of the resistances, capacitors, and inductors in the EC.

Consider a PSC that shows an amount of hysteresis when $J-V$ is measured by a cycling method, as indicated in the top box of Figure 12. We also have obtained the impedance spectra at different points of the quasi-stationary curve as indicated in the left diagram. We assume that we have determined an EC that describes the spectra over the whole voltage range of interest. We have also characterized the voltage dependence of parameters. Examples of such type of data information are in Figure 3c,d and later on Figure 20.

Now we apply a method that converts the EC into a set of dynamical equations for the relevant variables in the system:

$V$, the voltage at the contacts. This is the external input variable that we can program according to the chosen technique of measurement.

$I$, the current at the contacts. This is the external output variable.

$w_1$, $w_2$, $w_3$, ... Internal state variables.

The effect of the internal variables on a general curve with memory effect $I(V,w)$ is shown in Figure 2b. The system's

evolution depends not only on the present state of the external input $V$ but also on the evolution of the internal variables $w_i$.

Therefore, from the EC model, we can derive a set of differential equations where the voltage-dependent circuit elements derived experimentally provide the coefficients in the equations. Then we can solve mathematically, either analytically or by a numerical integration, and we arrive at the output response $I(V)$ for the particular imposed trajectory of $V(t)$. This is the lower box in Figure 12. Finally, the theoretical scan-rate-dependent $J-V$ curves are then reconstructed and are correlated to the experimentally determined data. Using this approach, we obtain an independent description of the observed hysteresis. Furthermore, we can obtain an interpretation of the hysteresis by the effect of different elements in the EC, and we can investigate such elements independently to modify or improve the system's response in the time domain.
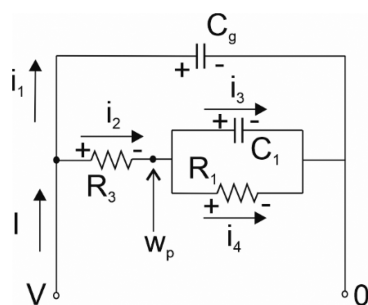
## 4. CAPACITIVE CIRCUIT MODEL

### 4.1. Converting the Equivalent Circuit to Time Domain Equations

We describe the method to systematically convert the equations for the currents and voltages in the EC into a set of first order differential equations. We explain the method applied to the standard circuit of the PSC in Figure 4, as shown in Figure 13. The node voltage method to solve a circuit will provide the required structure of equations in the frequency domain. It has the following steps:

 (i) Assign a reference node.
 (ii) Assign node voltage names to the remaining nodes.
 (iii) Write Kirchhoff's current law for each node.
 (iv) Manipulate the equations to the required form that will provide kinetic equations in the time domain.

Note that currents and voltages in Figure 13 bear a tilde (not shown in the figure) since they correspond to the small amplitude of IS measurements. The zero node is at the right-hand side in Figure 13. The external voltage $\tilde{V}$ determines one node, and the external current is $\tilde{I}$. The other node is assigned

**Figure 13.** Application of the node voltages method to solve the capacitive circuit of Figure 5.

a voltage $\tilde{w}_p$. This is the single internal state variable. We write the Kirchhoff equations for the two nodes. The result is

$$\tilde{I} = sC_g\tilde{V} + \frac{1}{R_3}(\tilde{V} - \tilde{w}_p) \tag{17}$$

$$\frac{1}{R_3}(\tilde{V} - \tilde{w}_p) = sC_1\tilde{w}_p + \frac{\tilde{w}_p}{R_1} \tag{18}$$

When taking the transformation to the time domain, the product by $s$ gives the time derivative. We need to convert eqs 17 and 18 to a form in which each voltage is multiplied by $s$. By solving the equations, we find

$$sR_3C_g\tilde{V} = R_3\tilde{I} - (\tilde{V} - \tilde{w}_p) \tag{19}$$

$$sR_1C_1\tilde{w}_p = \frac{R_1}{R_3}\tilde{V} - \left(1 + \frac{R_1}{R_3}\right)\tilde{w}_p \tag{20}$$

Using the relaxation times introduced in eqs 9 and 10, we obtain the required differential equations in the time domain:

$$\tau_m\frac{d\tilde{V}}{dt} = R_3\tilde{I} - (\tilde{V} - \tilde{w}_p) \tag{21}$$

$$\tau_1\frac{d\tilde{w}_p}{dt} = \frac{R_1}{R_3}\tilde{V} - \left(1 + \frac{R_1}{R_3}\right)\tilde{w}_p \tag{22}$$

### 4.2. Steady-State Solution

Let us first analyze the steady state in which $dt \to \infty$. Then we have

$$\tilde{I} = \frac{1}{R_3}(\tilde{V} - \tilde{w}_p) \tag{23}$$

$$\tilde{w}_p = \frac{R_1}{R_1 + R_3}\tilde{V} \tag{24}$$

Therefore

$$\tilde{I} = \frac{1}{R_{dc}}\tilde{V} \tag{25}$$

At zero frequency, the impedance is the total resistance, as previously explained in eq 13. The dc resistance in eq 25 is

$$R_{dc} = R_1 + R_3 \tag{26}$$

### 4.3. General Method of Solution

The EC model of Figure 13 needs to be supplemented with the voltage dependence of the different elements. We use the exponential dependences in eqs 6–8. To simplify the problem,

we assume that the different elements have the same ideality factor $m_i = m$. The correlation of the voltage dependence of resistances and capacitances is a realistic assumption observed experimentally,[40,41] but this is not generally satisfied; see Figure 20.[53,55] The assumption $m_i = m$ allows us to solve completely the problem by analytical methods, without loss of generality. We thus have

$$R_1(V) = R_{10}e^{-V/V_m} \tag{27}$$

$$C_1(V) = C_{10}e^{V/V_m} \tag{28}$$

$$R_3(V) = R_{30}e^{-V/V_m} \tag{29}$$

where the ideality factor $m$ in terms of voltage is defined as

$$V_m = \frac{mk_BT}{q} \tag{30}$$

If the assumption in eqs 27–29 is not satisfied, then the whole process must be performed by numerical integration. For convenience, we define

$$r_0 = \frac{R_{10}}{R_{30}} \tag{31}$$

$$r_1 = 1 + r_0 \tag{32}$$

In order to continue the analysis toward a solution, we make a further simplification valid for slow measurements. As $\tau_m$ is quite short, as shown in Figure 3e, it is unlikely that we can observe the relaxation process associated with $R_3C_g$. Therefore, we remove the term with the time derivative in eq 21. This is equivalent to ignoring the geometrical capacitance $C_g$. On the other hand, the relaxation of $w_p$ is slow and will influence the measured $I{-}V$ curve, hence we leave the term with the derivative in eq 22. We obtain the equations

$$\tilde{I} = \frac{1}{R_3(\overline{V})}(\tilde{V} - \tilde{w}_p) \tag{33}$$

$$\tau_1\frac{d\tilde{w}_p}{dt} = \frac{R_1(\overline{V})}{R_3(\overline{V})}\tilde{V} - \left(1 + \frac{R_1(\overline{V})}{R_3(\overline{V})}\right)\tilde{w}_p \tag{34}$$

These two equations have the functional form of a memristive system:[38] eq 33 is the conductance equation depending on the internal memory variable $\tilde{w}_p$, and eq 34 describes the temporal evolution of the memory variable. Equations 21 and 22, or the more concrete form 33 and 34, must be solved combined for a given external perturbation $V(t)$ to provide the external current $I$. The external perturbation depends on the technique that is used: it could be a step voltage, a large sinusoidal, or any required form. For the $J{-}V$ hysteresis problem, we focus our interest in the voltage variation at a constant voltage sweep rate $v_0$ that is termed CV in electrochemistry, as described by eq 16. In the following sections, we will solve the current for CV technique. We will start with a description of the voltage ramp in the forward direction $(v_0 > 0)$.

For any possible specification of $V(t)$, we need to remark that the eqs 33 and 34 are not symmetric. The time dependence of $\tilde{w}_p$ can be obtained only from eq 34. Since $V(t)$ is known, only when $\tilde{w}_p(t)$ has been solved, then the solution of eq 33 can be attempted. Therefore, the process of integration begins with the equation for the memory variable(s).

### 4.4. Integration of the Memory Equation

We search the solution $I = I(V, v_0)$ starting with the eq 34 for the variable with memory $w_p$. For simplicity, we choose to work with the voltage $V$ as the independent variable, instead of time, since the state of the system is fixed by the instantaneous voltage by eq 16. We express the scan rate as

$$V_s = \tau_1 v_0 \tag{35}$$

and we can write

$$V_s \frac{d\tilde{w}_p}{dV} = r_0 \tilde{V} - r_1 \tilde{w}_p \tag{36}$$

An integration of the differential eq 36 starting at $V_0$ gives the evolution of $w_p(V)$ during a forward voltage scan:

$$w_p(V) = \left(-\frac{r_0}{r_1}V_0 + w_{p0} + \frac{r_0}{r_1^2}V_s\right)e^{-r_1/V_s(V-V_0)} + \frac{r_0}{r_1}V - \frac{r_0 V_s}{r_1^2} \tag{37}$$

### 4.5. Integration of the Conductance Equation: Steady-State Solution

The next and final step is the integration of eq 32 for a large amplitude voltage scan. First, let us assume that the variable $w_p$ reaches the equilibrium value in eq 24. Then the variation of $I$ expressed in eq 33 is

$$dI = \frac{1}{R_1(V) + R_3(V)} dV \tag{38}$$

This equation is the statement that the resistance is the derivative of the $I-V$ curve, as discussed in section 2.2. The integration from $V_0$ to $V$ given the initial current $I_0$ results to

$$I_s(V) = I_0 + \frac{V_m}{R_{10} + R_{30}}(e^{V/V_m} - e^{V_0/V_m}) \tag{39}$$

This is the stationary current–voltage curve, like eq 15, that is obtained at infinitely slow sweep velocity, or in any case in which the memory effects of $w_p$ can be neglected. $I_s(V)$ is shown in the blue curve of Figure 14. Equation 39 is also the current–voltage curve under illumination (with an added negative photocurrent).
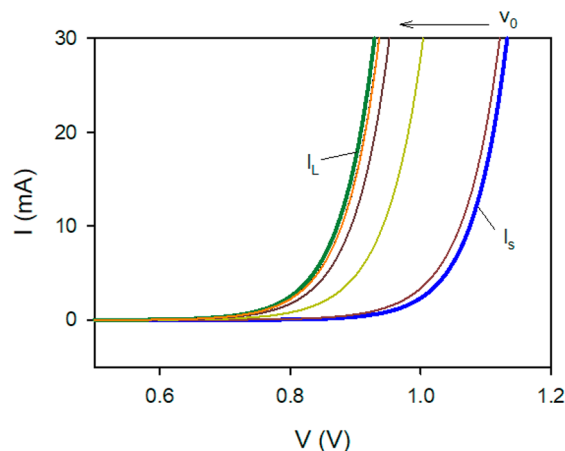


**Figure 14.** Stationary curve (eq 39) and current–voltage curves (eq 45) at different forward scan rates starting at $I(0) = 0$ for the capacitive circuit with parameters $R_{10} = 49 \times 10^5$ Ω, $R_{10} = 1 \times 10^5$ Ω, $r_1 = 50$, $\tau_1 = 1$ s, $C_{10} = 10^{-5}$ F, $k_B T = 0.026$ V, $m = 2$, $V_m = 0.052$ V, $V_s = \tau_1 v_0$ for $v_0 = 10^1, 10^{1.5}, 10^2, 10^{2.5}$ V/s.

### 4.6. Integration of the Conductance Equation: General Solution for the Current in a Forward Scan

We now proceed to the integration of eq 33 in the form of

$$dI = \frac{1}{R_3(V)}(dV - dw_p) \tag{40}$$

For the general case of an arbitrary sweep rate parameter $V_s$, we obtain the differential $dw_p$ in eq 40 from the second equation in our system, eq 36, resulting in

$$dw_p = \frac{r_0}{V_s} V dV - \frac{r_1}{V_s} w_p(V) dV \tag{41}$$

Inserting 41 into 40, we arrive at the equation

$$dI = \frac{1}{R_3(V)}dV - \frac{r_0}{R_3(V)V_s}VdV + \frac{r_1}{R_3(V)V_s}w_p(V)dV \tag{42}$$

Note that $w_p(V)$ is the state variable previously integrated in eq 37. Substituting it into eq 42 and with some algebraic manipulations, we obtain

$$dI = \frac{1}{R_1(V) + R_3(V)}dV + \frac{1}{R_3(V)}\left(\frac{r_0}{r_1} - \frac{r_0}{V_s}V_0 + \frac{r_1 w_{p0}}{V_s}\right)$$
$$e^{V/V_m - r_1/V_s(V-V_0)}dV \tag{43}$$

The first term on the right-hand side is the stationary curve in eq 38, with the integrated form given by eq 39 as $I_s(V)$. The second term in eq 43 is the current associated with the memory effect, $\Delta I(V_s, V)$. We, then, obtain

$$\Delta I(V_s, V) = \frac{1}{R_{30}}\frac{V_s}{\frac{V_s}{V_m} - r_1}\left(\frac{r_0}{r_1} - \frac{r_0}{V_s}V_0 + \frac{r_1 w_{p0}}{V_s}\right)$$
$$(e^{V/V_m - r_1/V_s(V-V_0)} - e^{V_0/V_m}) \tag{44}$$

The total current obtained by integration of eq 33 is the final solution to the integration method:

$$I(V) = I_s(V) + \Delta I(V_s, V) \tag{45}$$

The current at very large scan rate is

$$I_L = I_0 + \frac{1}{R_{30}}(e^{V/V_m} - e^{V/V_0}) \tag{46}$$

The large scan rate current $I_L$ is shown by the green trace in Figure 14. The calculated currents for different scan rates obtained by eq 45 are also presented in Figure 14. The excess current $\Delta I$ is positive in all cases; hence, the voltage at a reference current decreases as the scan rate increases. The current changes between the limits $I_S$ and $I_L$.

### 4.7. Interpretation of Forward Current in the Capacitive Circuit Model

The simple capacitive circuit explains the regular hysteresis in Figure 1a. Based on the solution of the problem, we can appreciate the general mechanism of hysteresis. At steady state, the effective resistance is $R_1 + R_3$, as indicated in eq 38, that describes the instantaneous ohmic behavior. However, if the system responds slowly to the external perturbation, $\tilde{w}_p$ remains small and $\tilde{I} \approx \tilde{V}/R_3$ in eq 33. This is because the capacitor is shorted at high frequency. Then the resistance is smaller, and the total resistive pathway contains only a fraction of $R_1$ in addition to $R_3$. The current is higher than at very slow

scan rate. This higher current is capacitive, as demonstrated in measurements.[75,76]

Figure 15 shows the evolution of voltage with sweep rate in two cases of the capacitive circuit with the same dc resistance
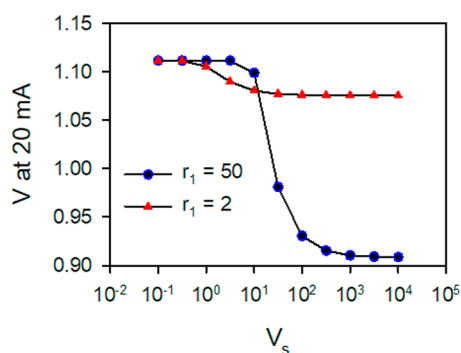


**Figure 15.** Forward scan rate dependence ($V_s = \tau_1 v_0$; $\tau_1 = 1$ s) of the voltage at $I = 20$ mA for two cases of the capacitive circuit with the same dc resistance $R_{dc0} = R_{10} + R_{30} = 10^6$ Ω.

defined by $R_{dc0} = R_{10} + R_{30}$. The voltage in equilibrium (slow scan rate) is the same in the two cases as they have the same total resistance. However, the voltage at $I = 20$ mA for higher scan rates is lower for the system with larger $R_1$. Therefore, the quotient of resistances $R_1/R_3$ is the main factor controlling the amount of regular hysteresis.

The onset of hysteresis as the scan rate increases occurs when the exponent in $\Delta I$ becomes positive, which is given by the condition
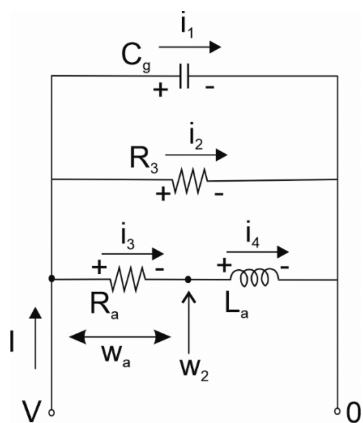
$$V_s > r_1 V_m \tag{47}$$

It can also be written in the form

$$v_0 > \left(\frac{1}{R_1} + \frac{1}{R_3}\right)\frac{1}{C_1}V_m \tag{48}$$

A large capacitance determines that the onset of hysteresis occurs at a low scan rate.

## 5. FORWARD CURRENT IN THE INDUCTIVE CIRCUIT MODEL

We apply the method of integration to the inductive circuit of Figure 7, according to the scheme illustrated in Figure 16.



**Figure 16.** Application of node voltage method to solve the inductive circuit of Figure 7.

We obtain the equations

$$\tilde{I} = sC_g\tilde{V} + \frac{1}{R_3(\overline{V})}\tilde{V} + \frac{1}{R_a(\overline{V})}(\tilde{V} - \tilde{w}_2) \tag{49}$$

$$\frac{1}{R_a(\overline{V})}(\tilde{V} - \tilde{w}_2) = \frac{1}{sL_a(\overline{V})}\tilde{w}_2 \tag{50}$$

This result is not what we expected because the $s$ in the second equation is in the denominator and will not produce a derivative term. However, since the equations are linear, we are free to produce linear combinations of the state variables. In this case, we choose the transformation

$$\tilde{w}_a = \tilde{V} - \tilde{w}_2 \tag{51}$$

Neglecting again the relaxation process associated with $R_3C_g$, we obtain

$$\tilde{I} = \frac{1}{R_3(\overline{V})}\tilde{V} + \frac{1}{R_a(\overline{V})}\tilde{w}_a \tag{52}$$

$$s\frac{L_a(\overline{V})}{R_a(\overline{V})}\tilde{w}_a = \tilde{V} - \tilde{w}_a \tag{53}$$

This last equation has the required form indicating that the physically meaningful state variable is the voltage $\tilde{w}_a$ in the resistor $R_a$ instead of the voltage in the inductor $\tilde{w}_2$.

We can express eq 53 in the time domain as

$$\tau_k\frac{d\tilde{w}_a}{dt} = \tilde{V} - \tilde{w}_a \tag{54}$$

where the kinetic constant is

$$\tau_k = \frac{L_a(\overline{V})}{R_a(\overline{V})} \tag{55}$$

This is the characteristic time of the inductive loop as shown in Figure 7.

In order to enable a relatively compact solution, we again assume that the voltage dependence of the EC elements is correlated with the same ideality factor $V_m$:

$$R_3(V) = R_{30}e^{-V/V_m} \tag{56}$$

$$R_a(V) = R_{a0}e^{-V/V_m} \tag{57}$$

$$L_a(V) = L_{a0}e^{-V/V_m} \tag{58}$$

It follows that $\tau_k$ in eq 55 is a constant.

In a steady-state situation, we obtain from eq 54

$$\tilde{w}_a = \tilde{V} \tag{59}$$

Therefore

$$\tilde{I} = \left(\frac{1}{R_3(\overline{V})} + \frac{1}{R_a(\overline{V})}\right)\tilde{V} \tag{60}$$

Correspondingly

$$dI = \frac{1}{R_{dc0}}e^{V/V_m}dV \tag{61}$$

where

$$\frac{1}{R_{dc0}} = \frac{1}{R_{30}} + \frac{1}{R_{a0}} \tag{62}$$

The stationary current is then

$$I_s = I_0 + \frac{V_m}{R_{dc0}}(e^{V/V_m} - e^{V_0/V_m}) \tag{63}$$

We focus our attention on the technique of CV. Defining

$$V_s = \tau_k v_0 \tag{64}$$

Equation 54 turns into

$$V_s \frac{d\tilde{w}_a}{dV} = \tilde{V} - \tilde{w}_a \tag{65}$$

By integration of this last equation, we find the evolution of the memory variable

$$w_a(V) = V - V_s + (w_{a0} - V_0 + V_s)e^{(V_0-V)/V_s} \tag{66}$$

Now we aim to integrate eq 52

$$dI = \frac{1}{R_3(V)}dV + \frac{1}{R_a(V)}dw_a \tag{67}$$

We use eq 54 as follows:

$$dw_a = \frac{1}{V_s}(V - w_a)dV \tag{68}$$

Substituting into eq 67

$$dI = \frac{1}{R_3(V)}dV + \frac{1}{R_a(V)}dV - \frac{1}{V_s R_a(V)}$$
$$[V - V_s + (w_{a0} - V_0 + V_s)e^{(V_0-V)/V_s}]dV \tag{69}$$

The total current is

$$I(V) = I_s(V) + \Delta I(V_s, V) \tag{70}$$

where

$$\Delta I = -\frac{V_s + w_{a0} - V_0}{R_{a0}} \frac{1}{\frac{V_s}{V_m} - 1}(e^{V_0/V_s + (1/V_m - 1/V_s)V} - e^{V_0/V_m}) \tag{71}$$

The current at very large scan rate is

$$I_L = \frac{V_m}{R_{30}}(e^{V/V_m} - 1) \tag{72}$$

The current−voltage curves at varying forward scan rates with $I_S$ and $I_L$ for the inductive circuit are shown in Figure 17. The onset of hysteresis as the scan rate increases occurs when the exponent in $\Delta I$ becomes positive, which is given by the condition

$$V_s > V_m \tag{73}$$

It can also be written in the form

$$v_0 > \frac{V_m}{\tau_k} \tag{74}$$

When hysteresis is significant at high scan rate, the current $\Delta I$ in this model is negative. Therefore, the inductor branch explains the inverted hysteresis, which gives a sound ground to the observations in ref 80. Consistently, the current moves between two limiting curves, from $I_S$ toward $I_L$, at large sweep rates. At high frequencies, the inductor branch is an open circuit, and the current at high scan rate is determined by $R_3$. At low scan rates, the inductor branch becomes active and the current is reduced by the parallel pathway $R_a$. The extent of
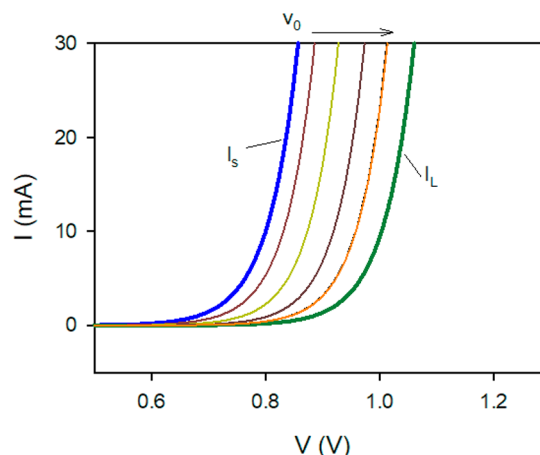


**Figure 17.** Stationary curve (eq 63) and current−voltage curves (eq 70) at different forward scan rates starting at $I(0) = 0$ and $w_a = 0$ for the inductive circuit with the parameters $R_{dc0} = 2.5 \times 10^4 \, \Omega$, $R_{10} = 50/49 \, R_{dc0}$, $R_{30} = 50 \, R_{dc0}$, $\tau_k = 11$ s, $k_B T = 0.026$ V, $m = 2$, $V_m = 0.052$ V, $V_s = \tau_k v_0$ for $v_0 = 10^1, 10^{1.5}, 10^2, 10^{2.5}$ V/s.

hysteresis depends again on the relative size of resistances $R_a/R_3$, as shown in Figure 18, for two cells with the same dc
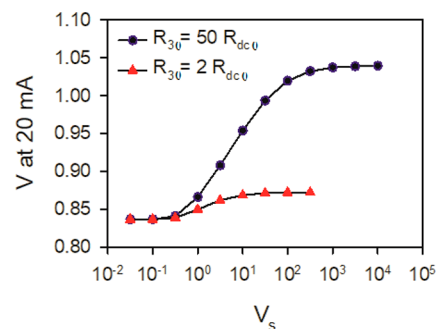


**Figure 18.** Forward scan rate dependence ($V_s = \tau_k v_0$; $\tau_k = 1$ s) of the voltage at $I = 20$ mA for two cases of the inductive circuit with the same dc resistance $R_{dc0} = 2.5 \times 10^4 \, \Omega$.

characteristics. Moreover, the integration of the IS EC model to predict the evolution of the current−voltage curves can also be implemented for reverse scan direction and under polarization effects (see the Supporting Information).

## 6. DISCUSSION

We have shown the transformation of the IS data to predict the evolution of current−voltage curves at different voltage sweep rates, revealing the origin of the hysteresis in certain capacitive and inductive elements in the EC. We have illustrated the method of integration using two elementary circuits that describe both types of hysteresis, regular and inverted, according to the time delay introduced by capacitive or inductive elements, respectively.

The method of integration is completely general. On the other hand, the specific models that we have solved are rather simple, e.g., by the assumption that all the elements have the same voltage dependence represented by the respective diode ideality factor $m$. Due to these simplifying assumptions, the models have been solved analytically and they provide certain conclusions regarding the kinetic constraints of hysteresis.
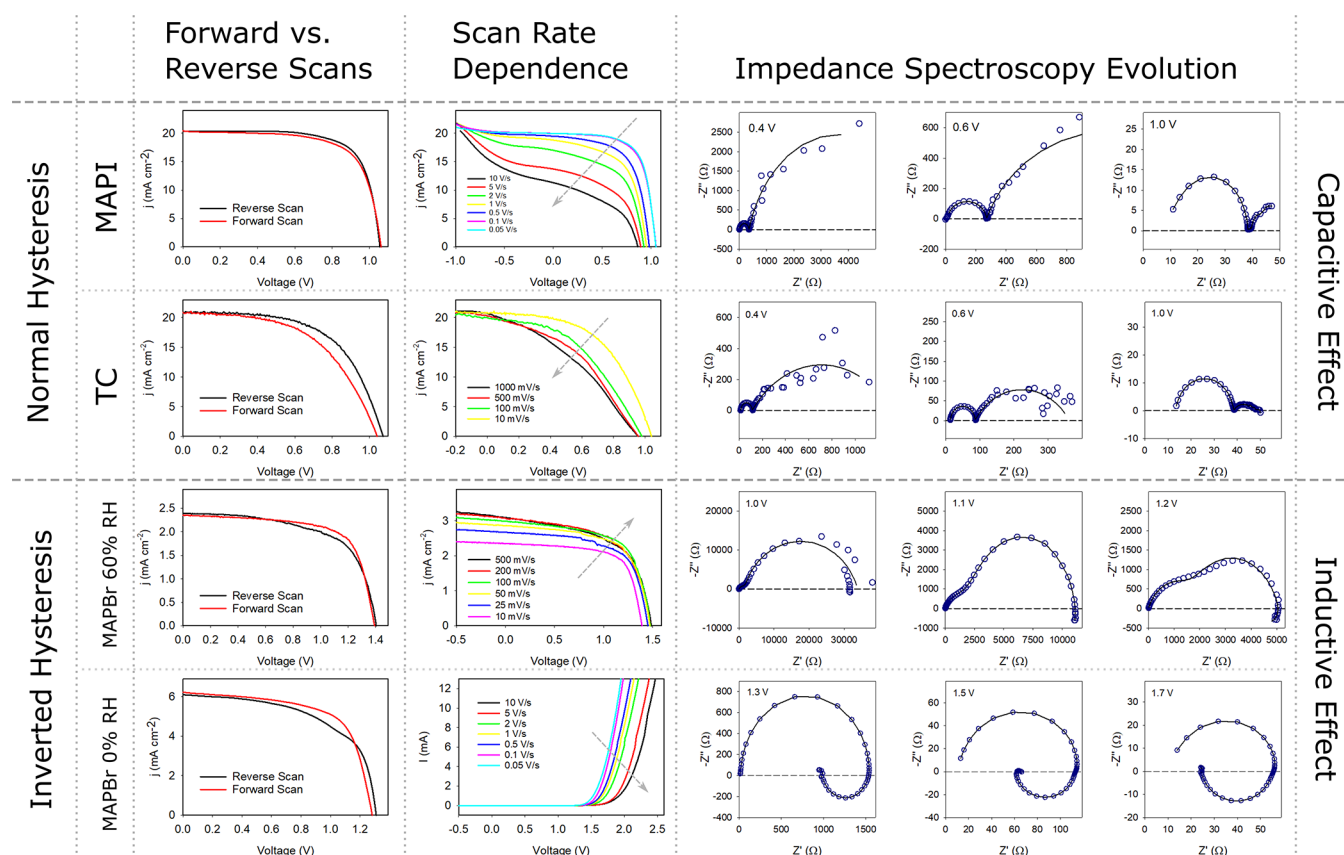
**Figure 19.** Catalogue of measured electrical response observed in our laboratories as a function of the perovskite formulation and measurement conditions. Normal hysteresis with capacitive response: MAPI and triple cation (TC) formulations. Inverted hysteresis with inductive response: MAPBr measured at RH = 60%[80] or in inert atmosphere (RH = 0%).

### 6.1. Conditions for Onset of Hysteresis

If an ac EC is made up of resistances only, the response to a voltage perturbation is immediate and there is no possible hysteresis. Delays are introduced by kinetic processes represented by capacitors and inductors. One can also associate certain time constants to the capacitive or inductive combination with resistors. Then, one finds that assessing the hysteresis entails a comparison of a voltage sweep rate, $v_0$ [V/s], and some characteristic time, $\tau$ [s].

However, these magnitudes have different units. How can they be compared? Our analysis shows that the diode quality factor represented in voltage units by $V_m$ is the essential quantity that enables the transformation from a voltage sweep rate to a pure time constant. Our study with a constant $V_m$ has provided clear criteria, involving a factor that compares the resistances in the system, for the presence of hysteresis: eq 48 for the capacitive circuit mode and eq 74 for the inductive circuit model.

### 6.2. Representative Experimental Behaviors

We are next set to illustrate some representative behaviors that have been observed in our research laboratories using different perovskite formulations. Figure 19 shows a catalogue of responses for different types of perovskite solar cells. We represent the observed hysteresis traces and the associated impedance responses at different voltages, separated by capacitive and inductive effect according to the above classification.

The general partition of types of hysteresis is well-supported by the IS data. First of all, we have consistently observed

normal hysteresis for devices measured under illumination conditions for compositions containing methylammonium lead iodide (MAPI) in the standard n−i−p structure or triple cation (TC, $FA_{0.85}$ $MA_{0.15}$ $Pb(I_{0.85}Br_{0.15})_3$). The normal hysteresis is clearly observed in the $J-V$ response as a function of the scan rate in which the $V_{oc}$ of the devices decreases with an increase in the scan rate during the forward scan. In agreement with the integration theory, the impedance spectra of these devices clearly show a capacitive response at low frequencies at different applied dc voltages.

Alternatively, a perovskite composition based on the methylammonium lead bromide (MAPBr) has been reported to show inverted hysteresis when the device is exposed to high relative humidity (RH = 60%).[80,85] The $J-V$ response as a function of the scan rate clearly shows that the $V_{oc}$ increases with the increase in the scan rate during forward scan. Impedance spectra measured in the dark in the range of 1.1−1.5 V show the appearance of the inductive effect which is responsible for the inverted hysteresis. We note that this inductive effect is not fully developed even at frequencies as low as 0.065 Hz for the reasons discussed below.

To further study this system, here we prepared fresh MAPBr cells following the method of ref 85. In this work, the MAPBr formulation has not been exposed to humid air, and devices are measured in inert atmosphere (RH = 0%). Interestingly, the $J-V$ curves measured in the dark also show inverted hysteresis as a function of the scan rates. In agreement with this result, the impedance spectra show an inductive arc which is fully developed touching the real $Z$ axis at low frequency. As it can
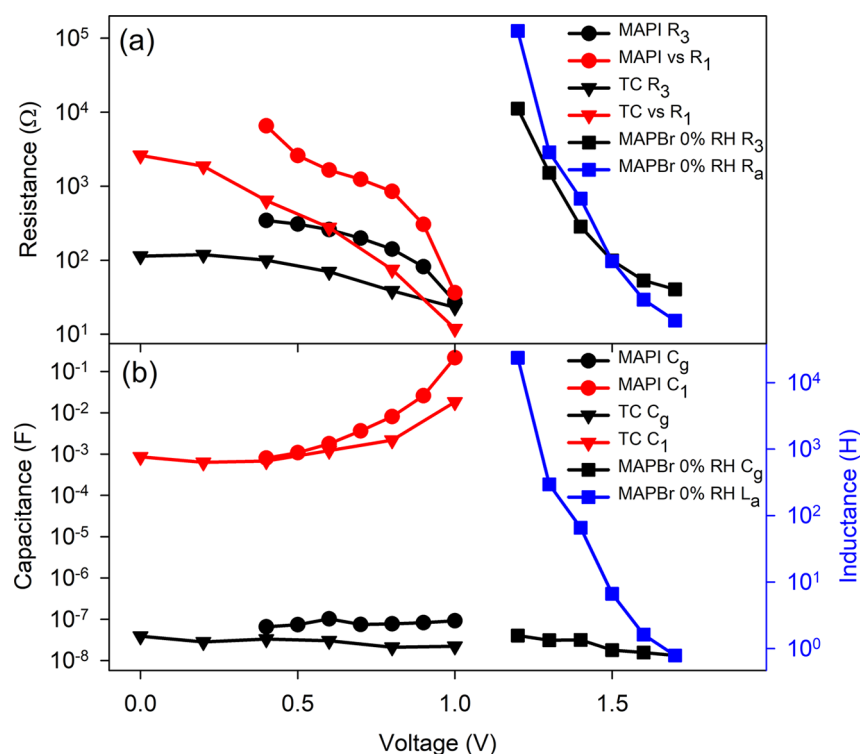
**Figure 20.** Summary of fitted (a) resistances, (b) capacitances and inductor of the ECs of Figures 4 and 7, extracted from the IS data of samples shown in Figure 19, represented as a function of the applied dc voltages.

be observed, hysteresis and impedance response are consistent with the methodology presented in this article.

### 6.3. Voltage Dependence of Resistances

The experimental data from samples described in Figure 19 are fitted to the ECs in Figures 4 and 7, depending on the capacitive or inductive characteristic of the spectrum. All impedance parameters are reported in the Supporting Information. The fitted parameters as a function of voltage are shown in Figure 20. We note that, in contrast to the naive models described in sections 4 and 5, the variable resistances are not exponential for most samples and they have different curvatures. In addition, we also observe some crossing of resistances $R_3$ with $R_1$ and $R_a$ for MAPI and MAPBr, respectively.

The lack of voltage-dependent linear response of resistances in the semilog plot is related to the question of the diode quality factor in PSCs that has been amply discussed in the literature. In principle, with ideal contacts and well-defined recombination mechanism, one can obtain a single constant $m$ value.[44] In fact, when the measurements are carried out at variable illumination and $V_{oc}$ conditions, resistances in PSC show a well-behaved exponential variation, as shown in Figure 3. The constant ideality factor in terms of voltage, $V_m$, over extended voltage ranges, often reported in the literature, has been typically obtained by measurement of different points at open-circuit potential.[44,49,54,55,86] However, the recombination mechanisms are often not ideal,[87] and the continuous application of an external voltage may induce chemical and structural changes in the perovskite composition. It is well-known that tracking the dark $J-V$ curve produces a strongly voltage-dependent ideality factor.[86,88,89] Therefore, the simple models that have been adopted to illustrate integration theory cannot directly be translated to the interpretation of measure-

ments. Nevertheless, we can infer some conclusions from the previous results. It was shown that the $J-V$ curve changes between two limits, from very slow to very fast scan rate (Figures 14 and 17). Each limit curve corresponds to a specific combination of resistances: a capacitor shorts the parallel resistance at high frequency, while the inductor activates its series resistance at low frequency. Correspondingly, in general, the diode exponent $m$ is a variable element depending on scan rate: it will be determined by a certain combination of resistances at low frequency and a different combination at high frequency. If the resistances have different exponential dependences with respect to voltage, then the actual ideality factor of the $J-V$ curve will be variable with voltage, as observed experimentally.[89] A preliminary model with the different exponents for slow and fast modes of the resistance was shown in ref 68.

### 6.4. Kinetic Time Constants

Using the results of the fitting, it is possible to calculate the response time for the slow capacitive relaxation phenomenon ($\tau_1$) and the kinetic constant that leads to the inductive effect ($\tau_k$). As can be observed in Figure 21, the response is highly dependent on the perovskite composition, with longer times (associated with lower frequency response) for MAPI ($\tau_1 \sim 5-10$ s) compared to those with the TC formulation ($\tau_1 \sim 0.1-1$ s). Similarly, the effect of ambient water on the kinetics of the inductive response is remarkable. In the case of MAPbBr$_3$ measured at RH = 60%, the inductive arc is only incipient with the lowest frequency data point measured that corresponds to a frequency $\omega = 0.41$ rad/s, with a corresponding $\tau_k$ longer than 2.4 s. This is consistent with the first reported determinations of $\tau_k$ between 20 and 30 s.[67] As the arc does not close due to the experimental limitations (long measure-ment time), it will not be possible to obtain reliable extracted
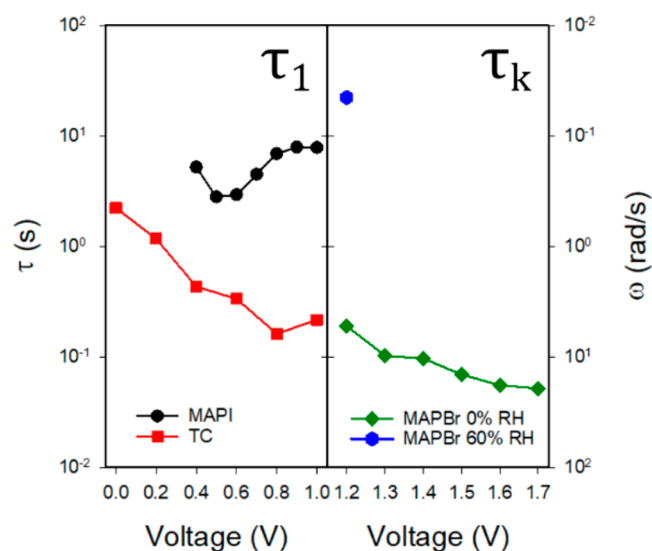
**Figure 21.** Response time for the slow capacitive relaxation phenomenon ($\tau_1$) and the kinetic constant that leads to the inductive effect ($\tau_k$) calculated from the fitted IS parameters obtained from the samples in Figure 19.



**Figure 22.** Forward scan $J-V$ curves measured in the dark and at different rates for a MAPBr solar cell (RH = 0%) and impedance response at voltages below the crossing point.

values for $R_a$ and $L_a$, due to the fact that $\tau_k$ is at the edge of the measuring window of frequencies, as shown in Figure 21. Alternatively, for MAPbBr measured in a glovebox (RH = 0%), the time response of the inductive phenomenon is fast, with values in the range of $\tau_k \sim 0.01-0.1$ s. This fast response makes it possible to observe a fully developed inductive arc that closes within the measurement time: the typical range of measurement can capture it, and the good stability of the cell avoids interference of noise.[90]

### 6.5. Transformation of the Equivalent Circuit along the Variation of Voltage

Finally, we comment on a peculiar behavior of PSCs that consists on *the change of the equivalent circuit*, from capacitive to inductive, as the dc voltage is varied. This transformation leads to a change of the hysteresis response in a single $J-V$ curve, as predicted by the integration theory. This transformation has been observed in the impedance response of memristors, as shown in Figure 6.[57] Here, we report the impact on the shape of the $J-V$ curve. Indeed, PSCs containing MAPBr measured in the dark and in the absence of ambient humidity (RH = 0%) show this mixed behavior, as shown in Figure 22. The same $J-V$ curve described in Figure 19 is replotted using a semilog scale, and we observe that the scans at different scan rates have a crossing point at approximately 1.2 V. At high voltages, the inverted hysteresis is observed as previously mentioned. In contrast, the baseline current at 0 V changes more than 1 order of magnitude with a capacitive response in this voltage range, in which the current increases with scan rate as expected in the elementary models of capacitive current.[78] Regarding the impedance spectroscopy data, in the capacitive regime at lower applied voltages, the spectra show the typical two arcs, and we can use the EC in Figure 4 to fit the data. On the other hand, the EC of Figure 7 fits the data at voltages above 1.2 V. In this voltage range, very well developed inductive arcs are observed. Indeed, the low-frequency arc and the inductive loop seem to be highly connected: as one decreases its magnitude as the other
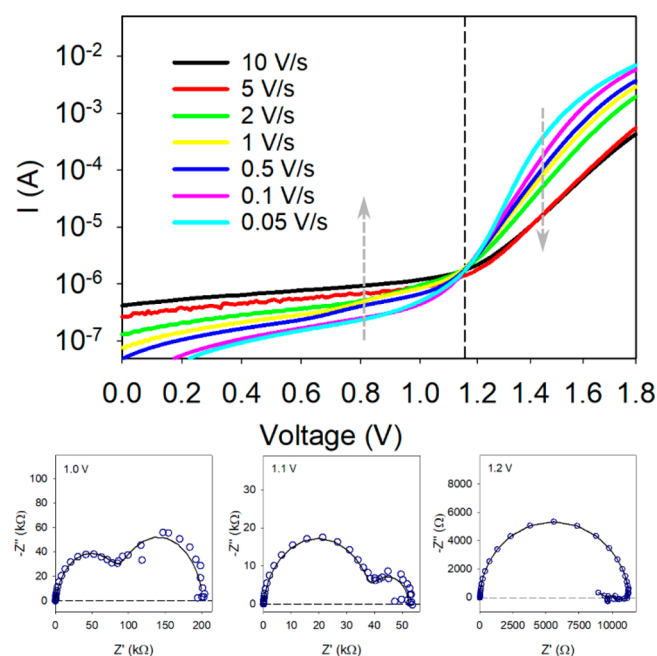
increases the weight in the response, as previously noted in Figure 6.

### 6.6. General Remarks and Limitations of the Method

In general, the IS analysis of PSCs shows processes much more complex than those used in our reference simple models.[91,92] The experimental quantity is the whole $Z(\omega)$ function while the decomposition into EC elements is a judgment of the experimenter. The resolution of the time domain processes in our integration method depends on the separation of the processes in the frequency domain. Integration over a wide voltage range using the relevant EC elements is necessary. Therefore, the description of experimental data will require the following:

(i) A sound EC that describes well the IS data over the voltage range of interest.

(ii) A numerical integration method to turn the differential equations into a time domain response.

We have emphasized the importance of the impedance spectroscopy analysis. We must not forget, however, that impedance $Z(\omega)$ is a two-port measurement and contains limited information about internal processes. One cannot expect a full picture of the internal variations. The complementary information should be attempted by combining other techniques.[93] It is well-established that dark- and light-induced processes provoke very different variations and conditions. The modifications of currents may be investigated by complementary light-modulated techniques.[94]

It is also important to note that if the current under an applied voltage scheme realizes a large excursion away from the steady-state line, the time- or voltage-dependent current data may not be well-obtained by integration of the linear impedance data as there are visited regions that lie far away from the steady-state $J-V$ curve. This is the case for a large reverse polarization[95] that introduces distinct phenomena such

as holes tunneling into the perovskite due to sharp band bending near the contact.[96]

## 7. CONCLUSION

Over the years, many regular properties of perovskite solar cells have emerged, and several phenomena have been consolidated and understood. However, an important uncertainty is how to deal with hysteresis that is deleterious for solar cells and, in practice, is often eliminated by trial and error. On the other hand, memristors show a magnified hysteresis effect that can be applied to resistive switching memories. Memristors have brought a new angle of analysis of hysteresis. They show a strong inverted hysteresis effect and indicate the pathway to relate hysteresis and impedance spectroscopy. We have built a method that, starting from IS data, is able to assess the amount of hysteresis that one may expect. The method works by turning the impedance spectroscopy model into a set of differential equations and integrating them for the required external voltage stimulus of the specific measurement technique. The system itself suggests the internal state variables, according to the complexity of the equivalent circuit: the number of internal variables corresponds to the number of internal nodes of the circuit. We solved two simple but relevant models. They show the physical reason for the dominant types of hysteresis reported in the literature: regular hysteresis is capacitive, whereas inverted hysteresis is inductive. Analysis of a variety of solar cells shows that the predicted properties are satisfied by the data. Moreover, we reported a system that undergoes transformation from capacitive to inductive hysteresis in a single $J-V$, governed by an equivalent circuit that undergoes transformation at a certain voltage. An analysis of more complex experimental data requires sophisticated methods involving the determination of the equivalent circuit by experimental analysis and the numerical integration of the differential equations.

## ASSOCIATED CONTENT

### Supporting Information

The Supporting Information is available free of charge at https://pubs.acs.org/doi/10.1021/acsphyschemau.1c00009.

Integration and interpretation for different polarization schedules, fitted impedance spectroscopy parameters (PDF)

## AUTHOR INFORMATION

### Corresponding Author

**Juan Bisquert** − *Institute of Advanced Materials (INAM), Universitat Jaume I, 12006 Castelló, Spain;* orcid.org/ 0000-0003-4987-4887; Email: bisquert@uji.es

### Authors

**Antonio Guerrero** − *Institute of Advanced Materials (INAM), Universitat Jaume I, 12006 Castelló, Spain;* orcid.org/0000-0001-8602-1248
**Cedric Gonzales** − *Institute of Advanced Materials (INAM), Universitat Jaume I, 12006 Castelló, Spain;* orcid.org/ 0000-0002-6550-2007

Complete contact information is available at:
https://pubs.acs.org/10.1021/acsphyschemau.1c00009

### Notes

The authors declare no competing financial interest.

## REFERENCES

(1) Snaith, H. J.; Abate, A.; Ball, J. M.; Eperon, G. E.; Leijtens, T.; Noel, N. K.; Stranks, S. D.; Wang, J. T.-W.; Wojciechowski, K.; Zhang, W. Anomalous Hysteresis in Perovskite Solar Cells. *J. Phys. Chem. Lett.* **2014**, *5*, 1511−1515.

(2) Unger, E. L.; Hoke, E. T.; Bailie, C. D.; Nguyen, W. H.; Bowring, A. R.; Heumüller, T.; Christoforo, M. G.; McGehee, M. D. Hysteresis and transient behavior in current-voltage measurements of hybrid-perovskite absorber solar cells. *Energy Environ. Sci.* **2014**, *7*, 3690−3698.

(3) Kim, H.-S.; Park, N.-G. Parameters Affecting I-V Hysteresis of $CH_3NH_3PbI_3$ Perovskite Solar Cells: Effects of Perovskite Crystal Size and Mesoporous $TiO_2$ Layer. *J. Phys. Chem. Lett.* **2014**, *5*, 2927−2934.

(4) van Reenen, S.; Kemerink, M.; Snaith, H. J. Modeling Anomalous Hysteresis in Perovskite Solar Cells. *J. Phys. Chem. Lett.* **2015**, *6*, 3808−3814.

(5) Kim, H.-S.; Jang, I.-H.; Ahn, N.; Choi, M.; Guerrero, A.; Bisquert, J.; Park, N.-G. Control of I-V Hysteresis in $CH_3NH_3PbI_3$ Perovskite Solar Cell. *J. Phys. Chem. Lett.* **2015**, *6*, 4633−4639.

(6) Almora, O.; Aranda, C.; Zarazua, I.; Guerrero, A.; Garcia-Belmonte, G. Noncapacitive Hysteresis in Perovskite Solar Cells at Room Temperature. *ACS Energy Lett.* **2016**, *1*, 209−215.

(7) Chen, B.; Yang, M.; Zheng, X.; Wu, C.; Li, W.; Yan, Y.; Bisquert, J.; Garcia-Belmonte, G.; Zhu, K.; Priya, S. Impact of capacitive effect and ion migration on the hysteretic behavior of perovskite solar cells. *J. Phys. Chem. Lett.* **2015**, *6*, 4693−4700.

(8) Rong, Y. G.; Hu, Y.; Ravishankar, S.; Liu, H. W.; Hou, X. M.; Sheng, Y. S.; Mei, A. Y.; Wang, Q. F.; Li, D. Y.; Xu, M.; Bisquert, J.; Han, H. W. Tunable hysteresis effect for perovskite solar cells. *Energy Environ. Sci.* **2017**, *10*, 2383−2391.

(9) Zimmermann, E.; Ehrenreich, P.; Pfadler, T.; Dorman, J. A.; Weickert, J.; Schmidt-Mende, L. Erroneous efficiency reports harm organic solar cell research. *Nat. Photonics* **2014**, *8*, 669−672.

(10) Christians, J. A.; Manser, J. S.; Kamat, P. V. Best Practices in Perovskite Solar Cell Efficiency Measurements. Avoiding the Error of Making Bad Cells Look Good. *J. Phys. Chem. Lett.* **2015**, *6*, 852−857.

(11) Wang, Y.; Liu, X.; Zhou, Z.; Ru, P.; Chen, H.; Yang, X.; Han, L. Reliable Measurement of Perovskite Solar Cells. *Adv. Mater.* **2019**, *31*, 1803231.

(12) Wu, F.; Pathak, R.; Qiao, Q. Origin and alleviation of J-V hysteresis in perovskite solar cells: A short review. *Catal. Today* **2021**, *374*, 86−101.

(13) Shao, Y.; Xiao, Z.; Bi, C.; Yuan, Y.; Huang, J. Origin and elimination of photocurrent hysteresis by fullerene passivation in $CH_3NH_3PbI_3$ planar heterojunction solar cells. *Nat. Commun.* **2014**, *5*, 5784.

(14) Peng, J.; Wu, Y.; Ye, W.; Jacobs, D. A.; Shen, H.; Fu, X.; Wan, Y.; Duong, T.; Wu, N.; Barugkin, C.; Nguyen, H. T.; Zhong, D.; Li, J.; Lu, T.; Liu, Y.; Lockrey, M. N.; Weber, K. J.; Catchpole, K. R.; White, T. P. Interface passivation using ultrathin polymer-fullerene films for high-efficiency perovskite solar cells with negligible hysteresis. *Energy Environ. Sci.* **2017**, *10*, 1792−1800.

(15) Duijnstee, E. A.; Ball, J. M.; Le Corre, V. M.; Koster, L. J. A.; Snaith, H. J.; Lim, J. Toward Understanding Space-Charge Limited Current Measurements on Metal Halide Perovskites. *ACS Energy Lett.* **2020**, *5*, 376−384.

(16) Azpiroz, J. M.; Mosconi, E.; Bisquert, J.; De Angelis, F. Defect migration in methylammonium lead iodide and its role in perovskite solar cell operation. *Energy Environ. Sci.* **2015**, *8*, 2118−2127.

(17) Lopez-Varo, P.; Jiménez-Tejada, J. A.; García-Rosell, M.; Ravishankar, S.; Garcia-Belmonte, G.; Bisquert, J.; Almora, O. Device Physics of Hybrid Perovskite Solar cells: Theory and Experiment. *Adv. Energy Mater.* **2018**, *8*, 1702772.

(18) Jacobs, D. A.; Wu, Y.; Shen, H.; Barugkin, C.; Beck, F. J.; White, T. P.; Weber, K.; Catchpole, K. R. Hysteresis phenomena in perovskite solar cells: the many and varied effects of ionic accumulation. *Phys. Chem. Chem. Phys.* **2017**, *19*, 3094−3103.

(19) Eames, C.; Frost, J. M.; Barnes, P. R. F.; O'Regan, B. C.; Walsh, A.; Islam, M. S. Ionic transport in hybrid lead iodide perovskite solar cells. *Nat. Commun.* **2015**, *6*, 7497.

(20) Calado, P.; Telford, A. M.; Bryant, D.; Li, X.; Nelson, J.; O'Regan, B. C.; Barnes, P. R. F. Evidence for ion migration in hybrid perovskite solar cells with minimal hysteresis. *Nat. Commun.* **2016**, *7*, 13831.

(21) Zhang, H.; Liang, C.; Zhao, Y.; Sun, M.; Liu, H.; Liang, J.; Li, D.; Zhang, F.; He, Z. Dynamic interface charge governing the current-voltage hysteresis in perovskite solar cells. *Phys. Chem. Chem. Phys.* **2015**, *17*, 9613−9618.

(22) Tress, W.; Marinova, N.; Moehl, T.; Zakeeruddin, S. M.; Nazeeruddin, M. K.; Gratzel, M. Understanding the rate-dependent J-V hysteresis, slow time component, and aging in $CH_3NH_3PbI_3$ perovskite solar cells: the role of a compensated electric field. *Energy Environ. Sci.* **2015**, *8*, 995−1004.

(23) Tress, W.; Correa Baena, J. P.; Saliba, M.; Abate, A.; Graetzel, M. Inverted Current-Voltage Hysteresis in Mixed Perovskite Solar Cells: Polarization, Energy Barriers, and Defect Recombination. *Adv. Energy Mater.* **2016**, *6*, 1600396.

(24) O'Regan, B. C.; Barnes, P. R. F.; Li, X.; Law, C.; Palomares, E.; Marin-Beloqui, J. M. Optoelectronic Studies of Methylammonium Lead Iodide Perovskite Solar Cells with Mesoporous $TiO2$: Separation of Electronic and Chemical Charge Storage, Understanding Two Recombination Lifetimes, and the Evolution of Band Offsets during J-V Hysteresis. *J. Am. Chem. Soc.* **2015**, *137*, 5087−5099.

(25) Richardson, G.; O'Kane, S. E. J.; Niemann, R. G.; Peltola, T. A.; Foster, J. M.; Cameron, P. J.; Walker, A. B. Can slow-moving ions explain hysteresis in the current-voltage curves of perovskite solar cells? *Energy Environ. Sci.* **2016**, *9*, 1476−1485.

(26) Seki, K. Equivalent circuit representation of hysteresis in solar cells that considers interface charge accumulation: Potential cause of hysteresis in perovskite solar cells. *Appl. Phys. Lett.* **2016**, *109*, 033905.

(27) Chen, T.; Sun, Z.; Liang, M.; Xue, S. Correlating hysteresis phenomena with interfacial charge accumulation in perovskite solar cells. *Phys. Chem. Chem. Phys.* **2020**, *22*, 245−251.

(28) Weber, S. A. L.; Hermes, I. M.; Turren-Cruz, S. H.; Gort, C.; Bergmann, V. W.; Gilson, L.; Hagfeldt, A.; Graetzel, M.; Tress, W.; Berger, R. How the formation of interfacial charge causes hysteresis in perovskite solar cells. *Energy Environ. Sci.* **2018**, *11*, 2404−2413.

(29) Courtier, N. E.; Cave, J. M.; Foster, J. M.; Walker, A. B.; Richardson, G. How transport layer properties affect perovskite solar cell performance: insights from a coupled charge transport/ion migration model. *Energy Environ. Sci.* **2019**, *12*, 396−409.

(30) Xiang, J.; Li, Y.; Huang, F.; Zhong, D. Effect of interfacial recombination, bulk recombination and carrier mobility on the J-V hysteresis behaviors of perovskite solar cells: a drift-diffusion simulation study. *Phys. Chem. Chem. Phys.* **2019**, *21*, 17836−17845.

(31) Akin, S. Hysteresis-Free Planar Perovskite Solar Cells with a Breakthrough Efficiency of 22% and Superior Operational Stability over 2000 h. *ACS Appl. Mater. Interfaces* **2019**, *11*, 39998−40005.

(32) Liu, Y.; Gao, Y.; Lu, M.; Shi, Z.; Yu, W. W.; Hu, J.; Bai, X.; Zhang, Y. Ionic additive engineering for stable planar perovskite solar cells with efficiency > 22%. *Chem. Eng. J.* **2021**, *426*, 130841.

(33) Yoo, J. J.; Seo, G.; Chua, M. R.; Park, T. G.; Lu, Y.; Rotermund, F.; Kim, Y.-K.; Moon, C. S.; Jeon, N. J.; Correa-Baena, J.-P.; Bulović, V.; Shin, S. S.; Bawendi, M. G.; Seo, J. Efficient perovskite solar cells via improved carrier management. *Nature* **2021**, *590*, 587−593.

(34) Wang, X.; Rakstys, K.; Jack, K.; Jin, H.; Lai, J.; Li, H.; Ranasinghe, C. S. K.; Saghaei, J.; Zhang, G.; Burn, P. L.; Gentle, I. R.;

Shaw, P. E. Engineering fluorinated-cation containing inverted perovskite solar cells with an efficiency of > 21% and improved stability towards humidity. *Nat. Commun.* **2021**, *12*, 52.

(35) Jeong, J.; Kim, M.; Seo, J.; Lu, H.; Ahlawat, P.; Mishra, A.; Yang, Y.; Hope, M. A.; Eickemeyer, F. T.; Kim, M.; Yoon, Y. J.; Choi, I. W.; Darwich, B. P.; Choi, S. J.; Jo, Y.; Lee, J. H.; Walker, B.; Zakeeruddin, S. M.; Emsley, L.; Rothlisberger, U.; Hagfeldt, A.; Kim, D. S.; Grätzel, M.; Kim, J. Y. Pseudo-halide anion engineering for α-FAPbI3 perovskite solar cells. *Nature* **2021**, *592*, 381−385.

(36) Aydin, E.; Liu, J.; Ugur, E.; Azmi, R.; Harrison, G. T.; Hou, Y.; Chen, B.; Zhumagali, S.; De Bastiani, M.; Wang, M.; Raja, W.; Allen, T. G.; Rehman, A. u.; Subbiah, A.; Babics, M.; Babayigit, A.; Isikgor, F.; Wang, K.; Van Kerschaver, E.; Tsetseris, L.; Sargent, E. H.; Laquai, F.; De Wolf, S. Ligand-bridged charge extraction and enhanced quantum efficiency enable efficient n-i-p perovskite/silicon tandem solar cells. *Energy Environ. Sci.* **2021**, DOI: 10.1039/D1EE01206A.

(37) Dorf, R. C.; Bishop, R. H. *Modern Control Systems*, 13th ed.; Pearson, 2017.

(38) Pershin, Y. V.; Di Ventra, M. Memory effects in complex materials and nanoscale systems. *Adv. Phys.* **2011**, *60*, 145−227.

(39) Kim, H.; Han, J. S.; Kim, S. G.; Kim, S. Y.; Jang, H. W. Halide perovskites for resistive random-access memories. *J. Mater. Chem. C* **2019**, *7*, 5226−5234.

(40) Harikesh, P. C.; Febriansyah, B.; John, R. A.; Mathews, N. Hybrid organic—inorganic halide perovskites for scaled-in neuromorphic devices. *MRS Bull.* **2020**, *45*, 641−648.

(41) Xiao, Z.; Huang, J. Energy-Efficient Hybrid Perovskite Memristors and Synaptic Devices. *Adv. Electron. Mater.* **2016**, *2*, 1600100.

(42) Wang, Y.; Lv, Z.; Chen, J.; Wang, Z.; Zhou, Y.; Zhou, L.; Chen, X.; Han, S.-T. Photonic Synapses Based on Inorganic Perovskite Quantum Dots for Neuromorphic Computing. *Adv. Mater.* **2018**, *30*, 1802883.

(43) Zhang, J.; Dai, S.; Zhao, Y.; Zhang, J.; Huang, J. Recent Progress in Photonic Synapses for Neuromorphic Systems. *Adv. Intell. Sys.* **2020**, *2*, 1900136.

(44) Correa-Baena, J.-P.; Turren-Cruz, S.-H.; Tress, W.; Hagfeldt, A.; Aranda, C.; Shooshtari, L.; Bisquert, J.; Guerrero, A. Changes from Bulk to Surface Recombination Mechanisms between Pristine and Cycled Perovskite Solar Cells. *ACS Energy Lett.* **2017**, *2*, 681−688.

(45) Fabregat-Santiago, F.; Garcia-Belmonte, G.; Mora-Seró, I.; Bisquert, J. Characterization of nanostructured hybrid and organic solar cells by impedance spectroscopy. *Phys. Chem. Chem. Phys.* **2011**, *13*, 9083−9118.

(46) von Hauff, E. Impedance Spectroscopy for Emerging Photovoltaics. *J. Phys. Chem. C* **2019**, *123*, 11329−11346.

(47) Wang, H.; Guerrero, A.; Bou, A.; Al-Mayouf, A. M.; Bisquert, J. Kinetic and material properties of interfaces governing slow response and long timescale phenomena in perovskite solar cells. *Energy Environ. Sci.* **2019**, *12*, 2054−2079.

(48) Johnston, M. B.; Herz, L. M. Hybrid Perovskites for Photovoltaics: Charge-Carrier Recombination, Diffusion, and Radiative Efficiencies. *Acc. Chem. Res.* **2016**, *49*, 146−154.

(49) Zarazua, I.; Han, G.; Boix, P. P.; Mhaisalkar, S.; Fabregat-Santiago, F.; Mora-Seró, I.; Bisquert, J.; Garcia-Belmonte, G. Surface Recombination and Collection Efficiency in Perovskite Solar Cells from Impedance Analysis. *J. Phys. Chem. Lett.* **2016**, *7*, 5105−5113.

(50) Guerrero, A.; Garcia-Belmonte, G.; Mora-Sero, I.; Bisquert, J.; Kang, Y. S.; Jacobsson, T. J.; Correa-Baena, J.-P.; Hagfeldt, A. Properties of Contact and Bulk Impedances in Hybrid Lead Halide Perovskite Solar Cells Including Inductive Loop Elements. *J. Phys. Chem. C* **2016**, *120*, 8023−8032.

(51) Kim, S.-G.; Li, C.; Guerrero, A.; Yang, J.-M.; Zhong, Y.; Bisquert, J.; Huettner, S.; Park, N.-G. Potassium ions as a kinetic controller in ionic double layers for hysteresis-free perovskite solar cells. *J. Mater. Chem. A* **2019**, *7*, 18807−18815.

(52) Peng, W.; Aranda, C.; Bakr, O. M.; Garcia-Belmonte, G.; Bisquert, J.; Guerrero, A. Quantification of Ionic Diffusion in Lead

Halide Perovskite Single Crystals. *ACS Energy Lett.* **2018**, *3*, 1477−1481.

(53) Almora, O.; Cho, K. T.; Aghazada, S.; Zimmermann, I.; Matt, G. J.; Brabec, C. J.; Nazeeruddin, M. K.; Garcia-Belmonte, G. Discerning recombination mechanisms and ideality factors through impedance analysis of high-efficiency perovskite solar cells. *Nano Energy* **2018**, *48*, 63−72.

(54) Caprioglio, P.; Stolterfoht, M.; Wolff, C. M.; Unold, T.; Rech, B.; Albrecht, S.; Neher, D. On the Relation between the Open-Circuit Voltage and Quasi-Fermi Level Splitting in Efficient Perovskite Solar Cells. *Adv. Energy Mater.* **2019**, *9*, 1901631.

(55) Pockett, A.; Eperon, G. E.; Sakai, N.; Snaith, H. J.; Peter, L. M.; Cameron, P. J. Microseconds, milliseconds and seconds: deconvoluting the dynamic behaviour of planar perovskite solar cells. *Phys. Chem. Chem. Phys.* **2017**, *19*, 5959−5970.

(56) Solanki, A.; Guerrero, A.; Zhang, Q.; Bisquert, J.; Sum, T. C. Interfacial Mechanism for Efficient Resistive Switching in Ruddlesden-Popper Perovskites for Non-Volatile Memories. *J. Phys. Chem. Lett.* **2020**, *11*, 463−470.

(57) Gonzales, C.; Guerrero, A.; Bisquert, J. Spectral properties of the dynamic state transition in metal halide perovskite-based memristor exhibiting negative capacitance. *Appl. Phys. Lett.* **2021**, *118*, 073501.

(58) Dualeh, A.; Moehl, T.; Tétreault, N.; Teuscher, J.; Gao, P.; Nazeeruddin, M. K.; Grätzel, M. Impedance spectroscopic analysis of lead iodide perovskite-sensitized solid-state solar cells. *ACS Nano* **2014**, *8*, 362−373.

(59) Zohar, A.; Kedem, N.; Levine, I.; Zohar, D.; Vilan, A.; Ehre, D.; Hodes, G.; Cahen, D. Impedance Spectroscopic Indication for Solid State Electrochemical Reaction in $CH_3NH_3PbI_3$ Films. *J. Phys. Chem. Lett.* **2016**, *7*, 191−197.

(60) Fabregat-Santiago, F.; Kulbak, M.; Zohar, A.; Vallés-Pelarda, M.; Hodes, G.; Cahen, D.; Mora-Seró, I. Deleterious Effect of Negative Capacitance on the Performance of Halide Perovskite Solar Cells. *ACS Energy Lett.* **2017**, *2*, 2007−2013.

(61) Khan, M. T.; Huang, P.; Almohammedi, A.; Kazim, S.; Ahmad, S. Mechanistic origin and unlocking of negative capacitance in perovskites solar cells. *iScience* **2021**, *24*, 102024.

(62) Mora-Seró, I.; Bisquert, J.; Fabregat-Santiago, F.; Garcia-Belmonte, G.; Zoppi, G.; Durose, K.; Proskuryakov, Y. Y.; Oja, I.; Belaidi, A.; Dittrich, T.; Tena-Zaera, R.; Katty, A.; Lévy-Clement, C.; Barrioz, V.; Irvine, S. J. C. Implications of the negative capacitance observed at forward bias in nanocomposite and polycrystalline solar cells. *Nano Lett.* **2006**, *6*, 640−650.

(63) Klotz, D. Negative capacitance or inductive loop? - A general assessment of a common low frequency impedance feature. *Electrochem. Commun.* **2019**, *98*, 58−62.

(64) Taibl, S.; Fafilek, G.; Fleig, J. Impedance spectra of Fe-doped SrTiO3 thin films upon bias voltage: inductive loops as a trace of ion motion. *Nanoscale* **2016**, *8*, 13954−13966.

(65) Greenlee, J. D.; Calley, W. L.; Moseley, M. W.; Doolittle, W. A. Comparison of Interfacial and Bulk Ionic Motion in Analog Memristors. *IEEE Trans. Electron Devices* **2013**, *60*, 427−432.

(66) Pivac, I.; Šimić, B.; Barbir, F. Experimental diagnostics and modeling of inductive phenomena at low frequencies in impedance spectra of proton exchange membrane fuel cells. *J. Power Sources* **2017**, *365*, 240−248.

(67) Ghahremanirad, E.; Bou, A.; Olyaee, S.; Bisquert, J. Inductive Loop in the Impedance Response of Perovskite Solar Cells Explained by Surface Polarization Model. *J. Phys. Chem. Lett.* **2017**, *8*, 1402−1406.

(68) Ravishankar, S.; Almora, O.; Echeverría-Arrondo, C.; Ghahremanirad, E.; Aranda, C.; Guerrero, A.; Fabregat-Santiago, F.; Zaban, A.; Garcia-Belmonte, G.; Bisquert, J. Surface Polarization Model for the Dynamic Hysteresis of Perovskite Solar Cells. *J. Phys. Chem. Lett.* **2017**, *8*, 915−921.

(69) Jacobs, D. A.; Shen, H.; Pfeffer, F.; Peng, J.; White, T. P.; Beck, F. J.; Catchpole, K. R. The Two Faces of Capacitance: New Interpretations for Electrical Impedance Measurements of Perovskite

Solar Cells and their Relation to Hysteresis. *J. Appl. Phys.* **2018**, *124*, 225702.

(70) Moia, D.; Gelmetti, I.; Calado, P.; Fisher, W.; Stringer, M.; Game, O.; Hu, Y.; Docampo, P.; Lidzey, D.; Palomares, E.; Nelson, J.; Barnes, P. R. F. Ionic-to-electronic current amplification in hybrid perovskite solar cells: ionically gated transistor-interface circuit model explains hysteresis and impedance of mixed conducting devices. *Energy Environ. Sci.* **2019**, *12*, 1296−1308.

(71) Ebadi, F.; Taghavinia, N.; Mohammadpour, R.; Hagfeldt, A.; Tress, W. Origin of Apparent Light-Enhanced and Negative Capacitance in Perovskite Solar Cells. *Nat. Commun.* **2019**, *10*, 1574.

(72) Choi, W.; Song, S. W.; Han, S. G.; Cho, K. The Origin of Photoinduced Capacitance in Perovskite Solar Cells: Beyond Ionic-to-Electronic Current Amplification. *Adv. Electron. Mater.* **2020**, *6*, 2000030.

(73) Fletcher, S. Tables of Degenerate Electrical Networks for Use in the Equivalent-Circuit Analysis of Electrochemical Systems. *J. Electrochem. Soc.* **1994**, *141*, 1823−1826.

(74) Sanchez, R. S.; Gonzalez-Pedro, V.; Lee, J.-W.; Park, N.-G.; Kang, Y. S.; Mora-Sero, I.; Bisquert, J. Slow dynamic processes in lead halide perovskite solar cells. Characteristic times and hysteresis. *J. Phys. Chem. Lett.* **2014**, *5*, 2357−2363.

(75) Garcia-Belmonte, G.; Bisquert, J. Distinction between Capacitive and Noncapacitive Hysteretic Currents in Operation and Degradation of Perovskite Solar Cells. *ACS Energy Lett.* **2016**, *1*, 683−688.

(76) Almora, O.; Zarazua, I.; Mas-Marza, E.; Mora-Sero, I.; Bisquert, J.; Garcia-Belmonte, G. Capacitive dark currents, hysteresis, and electrode polarization in lead halide perovskite solar cells. *J. Phys. Chem. Lett.* **2015**, *6*, 1645−1652.

(77) Jacobs, D. A.; Shen, H.; Pfeffer, F.; Peng, J.; White, T. P.; Beck, F. J.; Catchpole, K. R. The two faces of capacitance: New interpretations for electrical impedance measurements of perovskite solar cells and their relation to hysteresis. *J. Appl. Phys.* **2018**, *124*, 225702.

(78) Fabregat-Santiago, F.; Mora-Seró, I.; Garcia-Belmonte, G.; Bisquert, J. Cyclic voltammetry studies of nanoporous semiconductor electrodes. Models and application to nanocrystalline TiO2 in aqueous electrolyte. *J. Phys. Chem. B* **2003**, *107*, 758−769.

(79) Wu, F.; Pathak, R.; Chen, K.; Wang, G.; Bahrami, B.; Zhang, W.-H.; Qiao, Q. Inverted Current-Voltage Hysteresis in Perovskite Solar Cells. *ACS Energy Lett.* **2018**, *3*, 2457−2460.

(80) Alvarez, A. O.; Arcas, R.; Aranda, C. A.; Bethencourt, L.; Mas-Marzá, E.; Saliba, M.; Fabregat-Santiago, F. Negative Capacitance and Inverted Hysteresis: Matching Features in Perovskite Solar Cells. *J. Phys. Chem. Lett.* **2020**, *11*, 8417−8423.

(81) Scott, S. K. *Chemical Chaos*; Clarendon Press, 1991.

(82) Strogatz, S. H. *Nonlinear Dynamics and Chaos*, 2nd ed., CRC Press, 2019.

(83) Koper, M. T. M. Oscillations and Complex Dynamical Bifurcations in Electrochemical Systems. *Adv. Chem. Phys.* **2007**, *92*, 161.

(84) Koper, M. T. M. Non-linear phenomena in electrochemical systems. *J. Chem. Soc., Faraday Trans.* **1998**, *94*, 1369−1378.

(85) Aranda, C.; Guerrero, A.; Bisquert, J. Ionic Effect Enhances Light Emission and the Photovoltage of Methylammonium Lead Bromide Perovskite Solar Cells by Reduced Surface Recombination. *ACS Energy Lett.* **2019**, *4*, 741−746.

(86) Tress, W.; Yavari, M.; Domanski, K.; Yadav, P.; Niesen, B.; Correa Baena, J. P.; Hagfeldt, A.; Graetzel, M. Interpretation and evolution of open-circuit voltage, recombination, ideality factor and subgap defect states during reversible light-soaking and irreversible degradation of perovskite solar cells. *Energy Environ. Sci.* **2018**, *11*, 151−165.

(87) Wolff, C. M.; Caprioglio, P.; Stolterfoht, M.; Neher, D. Nonradiative Recombination in Perovskite Solar Cells: The Role of Interfaces. *Adv. Mater.* **2019**, *31*, 1902762.

(88) Wetzelaer, G.-J. A. H.; Scheepers, M.; Sempere, A. M.; Momblona, C.; Ávila, J.; Bolink, H. J. Trap-Assisted Non-Radiative

Recombination in Organic-Inorganic Perovskite Solar Cells. *Adv. Mater.* **2015**, *27*, 1837−1841.

(89) Courtier, N. E. Interpreting Ideality Factors for Planar Perovskite Solar Cells: Ectypal Diode Theory for Steady-State Operation. *Phys. Rev. Appl.* **2020**, *14*, 024031.

(90) Pitarch-Tena, D.; Ngo, T. T.; Vallés-Pelarda, M.; Pauporté, T.; Mora-Seró, I. Impedance Spectroscopy Measurements in Perovskite Solar Cells: Device Stability and Noise Reduction. *ACS Energy Lett.* **2018**, *3*, 1044−1048.

(91) Ravishankar, S.; Aranda, C.; Sanchez, S.; Bisquert, J.; Saliba, M.; Garcia-Belmonte, G. Perovskite Solar Cell Modeling Using Light and Voltage Modulated Techniques. *J. Phys. Chem. C* **2019**, *123*, 6444−6449.

(92) Bou, A.; Pockett, A.; Raptis, D.; Watson, T.; Carnie, M. J.; Bisquert, J. Beyond Impedance Spectroscopy of Perovskite Solar Cells: Insights from the Spectral Correlation of the Electrooptical Frequency Techniques. *J. Phys. Chem. Lett.* **2020**, *11*, 8654−8659.

(93) Bergmann, V. W.; Guo, Y.; Tanaka, H.; Hermes, I. M.; Li, D.; Klasen, A.; Bretschneider, S. A.; Nakamura, E.; Berger, R.; Weber, S. A. L. Local Time-Dependent Charging in a Perovskite Solar Cell. *ACS Appl. Mater. Interfaces* **2016**, *8*, 19402−19409.

(94) Ravishankar, S.; Riquelme, A.; Sarkar, S. K.; Garcia-Batlle, M.; Garcia-Belmonte, G.; Bisquert, J. Intensity-Modulated Photocurrent Spectroscopy and Its Application to Perovskite Solar Cells. *J. Phys. Chem. C* **2019**, *123*, 24995−25014.

(95) Bowring, A. R.; Bertoluzzi, L.; O'Regan, B. C.; McGehee, M. D. Reverse Bias Behavior of Halide Perovskite Solar Cells. *Adv. Energy Mater.* **2018**, *8*, 1702365.

(96) Bertoluzzi, L.; Patel, J. B.; Bush, K. A.; Boyd, C. C.; Kerner, R. A.; O'Regan, B. C.; McGehee, M. D. Incorporating Electrochemical Halide Oxidation into Drift-Diffusion Models to Explain Performance Losses in Perovskite Solar Cells under Prolonged Reverse Bias. *Adv. Energy Mater.* **2021**, *11*, 2002614.